ARTICLE OPEN

VCPIP1 drives diabetic cardiomyopathy by deubiquitinating AMPKγ1 and preventing AMPKα-γ subunit assembly in cardiomyocytes

Xue Han[1,2,3], Zhuqi Huang[4], Guoxuan Liu[1], Yanan Liu[1], Weiqi Li[1], Jianing Zheng[1], Jie Tong[1,2], Mingyang He[1], Yurou Wu[1], Ze Li[1], Wu Luo[3], Qiaojuan Shi[1], Huazhong Ying[1]✉ and Guang Liang[1,2,3]✉

Protein ubiquitination modifications contribute to cardiomyocyte homeostasis and pathophysiology in diabetic cardiomyopathy (DCM). Yet the roles of deubiquitinating enzymes (DUBs) in DCM remain poorly defined. This study sought to delineate how valosin-containing protein interacting protein 1 (VCPIP1), a DUB, regulates DCM and to explore the molecular basis involved. We identify that VCPIP1 was significantly elevated in diabetic hearts, and upregulated VCPIP1 was mainly distributed in cardiomyocytes. Knockout of VCPIP1 specifically in cardiomyocytes ameliorated cardiac damage in mouse models of both type 2 and type 1 diabetes. Ubiquitinome and interactome profiling revealed AMPKγ1 as a substrate of VCPIP1 in cardiomyocytes. Mechanistically, VCPIP1 binds the cystathionine-β-synthase 2 domain of AMPKγ1 via its UBX-L domain and then catalyzes the K63-linked deubiquitination of AMPKγ1-K234 site through its catalytic residue C218. This VCPIP1-mediated AMPKγ1 deubiquitination disrupts AMPKα-γ heterodimer integrity, allosterically impairing AMPKα2-LKB1 interaction and limiting LKB1-mediated AMPKα^{T172} phosphorylation. RNA-seq analysis showed that AMPKγ1-K234 deubiquitination impaired mitochondrial respiration through inactivating AMPKα in cardiomyocytes, while VCPIP1 deficiency reversed hyperglycemia-induced mitochondrial dysfunction. Finally, AMPKγ1-K234R mutant phenocopied VCPIP1-mediated cardiac pathology in *db/db* mice. In conclusion, our findings unveil the VCPIP1-AMPKγ1 axis as a non-canonical regulatory mechanism for AMPKα^{T172} phosphorylation in cardiomyocytes, suggesting that inhibition of VCPIP1 represents a novel treatment approach for DCM.

Signal Transduction and Targeted Therapy (2026)11:185 ; https://doi.org/10.1038/s41392-026-02701-9

INTRODUCTION

Diabetes mellitus (DM) presents a mounting global health burden.[1] Cardiovascular complications drive the overwhelming majority of diabetes-related mortality, where hidden myocardial injury causes most fatalities.[2] Diabetic cardiomyopathy (DCM), defined as ventricular dysfunction unexplained by conventional cardiovascular etiologies, remains critically underdiagnosed, affecting approximately 14.5% of type 1 DM (T1DM) and 35.0% of type 2 DM (T2DM) populations.[3,4] Heart failure incidence is substantially elevated in diabetic patients relative to non-diabetic counterparts.[5] Therapeutically, while sodium-glucose cotransporter 2 (SGLT-2) inhibitors and glucagon-like peptide-1 (GLP-1) receptor agonists exhibit cardioprotective properties,[6] no consensus exists regarding optimal strategies for DCM management. It is imperative for deeper mechanistic insights to develop targeted therapies for DCM.

DCM is intrinsically linked to profound mitochondrial dysfunction, driven by chronic hyperglycemia and metabolic dysregulation.[7] Cardiac mitochondria, responsible for more than 90% cardiomyocyte ATP via oxidative phosphorylation (OXPHOS), suffer multifaceted damage in diabetes and diminished ATP synthesis.[8,9] This energetic deficit, manifested as inefficient energy supply, propels adverse cardiac remodeling, featuring systolic impairment, hypertrophy, and fibrosis.[10] Evidence indicates that compromised bioenergetic efficiency in diabetic cardiac mitochondria primarily attributed to respiration deficits across complexes I, II, and IV alongside depleted thioredoxin-2/glutathione antioxidant reservoirs.[11] Crucially, AMP-activated protein kinase (AMPK), which functions as a central governor of cellular energy balance, is significantly suppressed in diabetic hearts, directly contributing to mitochondrial instability through diminished quality control and impaired OXPHOS efficiency.[12,13] Preclinical evidence demonstrates that AMPK activation restores mitochondrial complex I activity, reduces mtROS, and then attenuates cardiomyopathy in diabetic models.[14] Thus, positively regulating AMPK-mitochondrial axis represents a promising therapeutic strategy for DCM.

Cardiomyocytes, being terminally differentiated with scant regenerative capacity, rely critically on post-translational modifications (PTMs) to regulate their pathophysiological functions.[15]

[1]Zhejiang Provincial Key Laboratory of Drug Discovery and Safety Evaluation for Inflammatory Chronic Diseases, Laboratory Animal Center, Hangzhou Medical College, Hangzhou, China; [2]Zhejiang-Tailand Joint Laboratory of Cardiovascular Diseases, School of Pharmaceutical Sciences, Hangzhou Medical College, Hangzhou, China; [3]Department of Cardiology, the First Affiliated Hospital, Wenzhou Medical University, Wenzhou, China and [4]Department of Cardiology, Zhejiang Key Laboratory of Cardiovascular Intervention and Precision Medicine, Sir Run Run Shaw Hospital, Zhejiang University School of Medicine, Hangzhou, China
Correspondence: Huazhong Ying (yhz0101@126.com) or Guang Liang (wzmcliangguang@163.com)
These authors contributed equally: Xue Han, Zhuqi Huang

Received: 24 September 2025 Revised: 27 February 2026 Accepted: 17 March 2026
Published online: 18 May 2026

Ubiquitination and its reversal, deubiquitination, constitute a dynamic PTMs cycle that profoundly influences diverse cellular processes and disease pathogenesis by dictating the stability, activity, and localization of substrate proteins. E3 ligases mediate the ubiquitination process, whereas deubiquitinating enzymes (DUBs) are responsible for removing ubiquitin moieties from substrate proteins.[16,17] Human DUBs, numbering approximately 100 identified members, are primarily classified as cysteine proteases or metalloproteases.[18] Recently, our group focus on DUBs' regulatory mechanisms in cardiovascular pathogenesis, having identified several DUBs that attenuate hypertensive cardiac hypertrophy through stabilizing key proteins in cardiomyocytes.[19,20] Besides, *Xie* et al. have found that USP28 is involved in the progression of DCM via regulating PPARα-Mfn2 axis.[21] Nevertheless, how DUBs contributes to DCM pathogenesis is still poorly understood and deserves in-depth investigation to identify novel therapeutic targets.

Valosin-containing protein interacting protein 1 (VCPIP1), classified within the DUB family, contains an ovarian tumor domain (OTU) catalytic domain.[22] Beyond its originally described function in Golgi membrane reassembly during cell division via deubiquitinating p97/VCP-p47 complex, VCPIP1 has been further linked to DNA-protein crosslink resolution and modulation of oncogenic signaling cascades, including the Hippo-YAP pathway in cancer cells.[23,24] In the current study, through an analysis of public GEO databases, we identified significantly elevated VCPIP1 expression in cardiac tissues from both diabetic mouse models and human diabetic patients. The potential involvement of VCPIP1 in DCM warrants further investigation.

Subsequently, our study demonstrated that cardiomyocyte-specific deletion of VCPIP1 conferred cardioprotection in both T1DM and T2DM mouse models. Mechanistically, we revealed that VCPIP1 deubiquitinated AMPKγ1 at K234 site to negatively regulate AMPKα^{T172} phosphorylation and activity, thereby damaging mitochondrial energy homeostasis in cardiomyocytes. These findings reveal a novel VCPIP1-mediated AMPK regulatory mechanism in cardiomyocytes and suggest VCPIP1 as a promising therapeutic strategy for DCM.

RESULTS

Identification of cardiomyocyte-derived VCPIP1 involved in DCM progression

To delineate the expression landscape of DUBs in diabetic myocardium, we analyzed a published GEO dataset (GSE197999) from non-diabetic streptozocin (STZ)-induced diabetic animal hearts, and found that *Vcpip1* gene showed significant upregulation in diabetic hearts (Fig. 1a). Interestingly, another GEO dataset (GSE106177) from human samples also showed increased expression of this gene in heart tissues of T2DM patients (Fig. 1b). We further confirmed that *Vcpip1* transcript levels were significantly increased in both T2DM and T1DM myocardial tissues (Fig. 1c, d). Besides, the robust upregulation of VCPIP1 protein expression was observed in cardiac tissues from T2DM and T1DM mice (Fig. 1e, f). To determine the cellular source of increased VCPIP1 levels, we isolated primary cardiomyocytes and fibroblasts from neonatal rats. The time-course experiments revealed that high glucose plus palmitate (HG + PA) selectively upregulated VCPIP1 expression in primary cardiomyocytes (Fig. 1g), whereas HG + PA-challenged primary fibroblasts exhibited no detectable changes (Fig. 1h). The mRNA level of *Vcpip1* was elevated in HG + PA-challenged primary cardiomyocytes (Fig. 1i). Immunofluorescence staining showed that upregulated VCPIP1 was located in α-actinin-positive primary cardiomyocytes upon HG + PA stimulation (Fig. 1j). Similarly, double immunofluorescence staining using T2DM mouse heart tissues verified the elevated VCPIP1 predominant expression in the α-actinin-positive cardiomyocytes of diabetic heart tissues (Fig. 1k, l). These findings indicate cardiomyocyte VCPIP1 as a potential contributor to DCM pathogenesis.

VCPIP1 positively regulates hypertrophy in cardiomyocytes under diabetic condition

To examine the possible effect of VCPIP1 on cardiomyocyte pathology, silence or overexpression of this protein was applied in HG + PA-challenged primary cardiomyocytes. Transfection with VCPIP1 siRNA (siVCPIP1) markedly attenuated HG + PA-induced enlargement of cardiomyocyte area and upregulation of ANP and MyHC protein levels in primary cardiomyocytes (Fig. 2a, b). In contrast, overexpression of VCPIP1 via transfecting VCPIP1 plasmid (VCPIP1^{OE}) in primary cardiomyocytes aggravated HG + PA-induced hypertrophic phenotypes (Fig. 2c, d), indicating that VCPIP1 in cardiomyocytes promotes hypertrophy under hyperglycemic environment. We then examined if the DUB enzyme activity of VCPIP1 mediated its pro-hypertrophic ability. Since the cysteine at site 218 (C218) in VCPIP1 protein has been reported to be the critical residue for its deubiquitinating activity,[25] a catalytically inactive VCPIP1 mutant was generated by substituting cysteine 218 with alanine (C218A). As shown in Fig. 2e, f, the C218A mutant reversed the VCPIP1-mediated hypertrophic phenotypes in cardiomyocytes exposed to HG + PA, suggesting that the deubiquitinating activity of VCPIP1 regulates cardiomyocyte hypertrophy.

Cardiomyocyte-specific VCPIP1 knockout alleviates cardiomyopathy in both T2DM and T1DM mice

To establish cardiomyocyte-specific VCPIP1-deficient mice (VCPIP1 CKO), VCPIP1$^{fl/fl}$ mice were crossed with Myh6-Cre mice (Supplementary Fig. 1a, b). Successful ablation of VCPIP1 in cardiomyocytes was confirmed by immunoblotting (Supplementary Fig. 1c). VCPIP1 CKO mice and their littermate VCPIP1$^{fl/fl}$ mice were fed a high fat diet (HFD) for 16 weeks combining low-dose STZ for 3 days to induce T2DM mouse model (Fig. 3a). Blood glucose, serum insulin, total cholesterol, and triglyceride levels remained comparable in T2DM mice with and without VCPIP1 knockout (Supplementary Fig.2a and Supplementary Table 1). As expected, echocardiographic assessment showed that VCPIP1 CKO mitigated systolic and diastolic dysfunction of diabetic heart, as reflected by increased E to A peak velocity ratio (E/A), ejection fraction (EF%), and fractional shortening (FS%), and decreased isovolumic relaxation time (IVRT), left ventricular internal diameter (LVIDd), and interventricular septal thickness (IVSD; Fig. 3b–e and Supplementary Table 1). Circulating ANP, a well-established biomarker of cardiac injury, exhibited significant reduction in diabetic mice with VCPIP1 CKO (Fig. 3f). VCPIP1 CKO also alleviated the T2DM-induced the enlargement of gross heart dimensions and elevation of the heart weight-to-body weight ratio (HW/BW; Fig. 3g, h). The degree of cardiomyocyte hypertrophy, as detected by hematoxylin and eosin (H&E) staining, wheat germ agglutinin (WGA) staining, and protein levels of ANP and MyHC, was significantly reversed by VCPIP1 CKO in T2DM mice (Fig. 3i–k). Moreover, the cardiac fibrosis measured by Masson's trichrome staining and Sirius red staining was significantly mitigated in VCPIP1-deficient diabetic mouse hearts (Fig. 3l and Supplementary Fig. 2b, c). Collectively, VCPIP1 ablation in cardiomyocytes attenuates DCM in T2DM mice.

We further employed a T1DM mouse model generated by high-dose STZ injection (60 mg/kg) for continuous 3 days (Supplementary Fig. 3a). STZ-treated mice manifested sustained hyperglycemia, while the blood glucose profile was not changed by VCPIP1 CKO (Supplementary Fig. 3b). VCPIP1 CKO markedly attenuated T1DM-induced cardiac dysfunction (Supplementary Fig. 3c–f and Table 2). Deletion of VCPIP1 in cardiomyocytes reversed T1DM-induced increase of serum ANP concentration (Supplementary Fig. 3g). T1DM mice exhibited marked cardiac abnormalities, including increased gross heart size, elevated HW/BW ratio, cardiomyocyte hypertrophy (evidenced by H&E and WGA staining), and upregulated ANP/MyHC protein expression, whereas VCPIP1 CKO prevented these pathological alterations (Supplementary Fig.

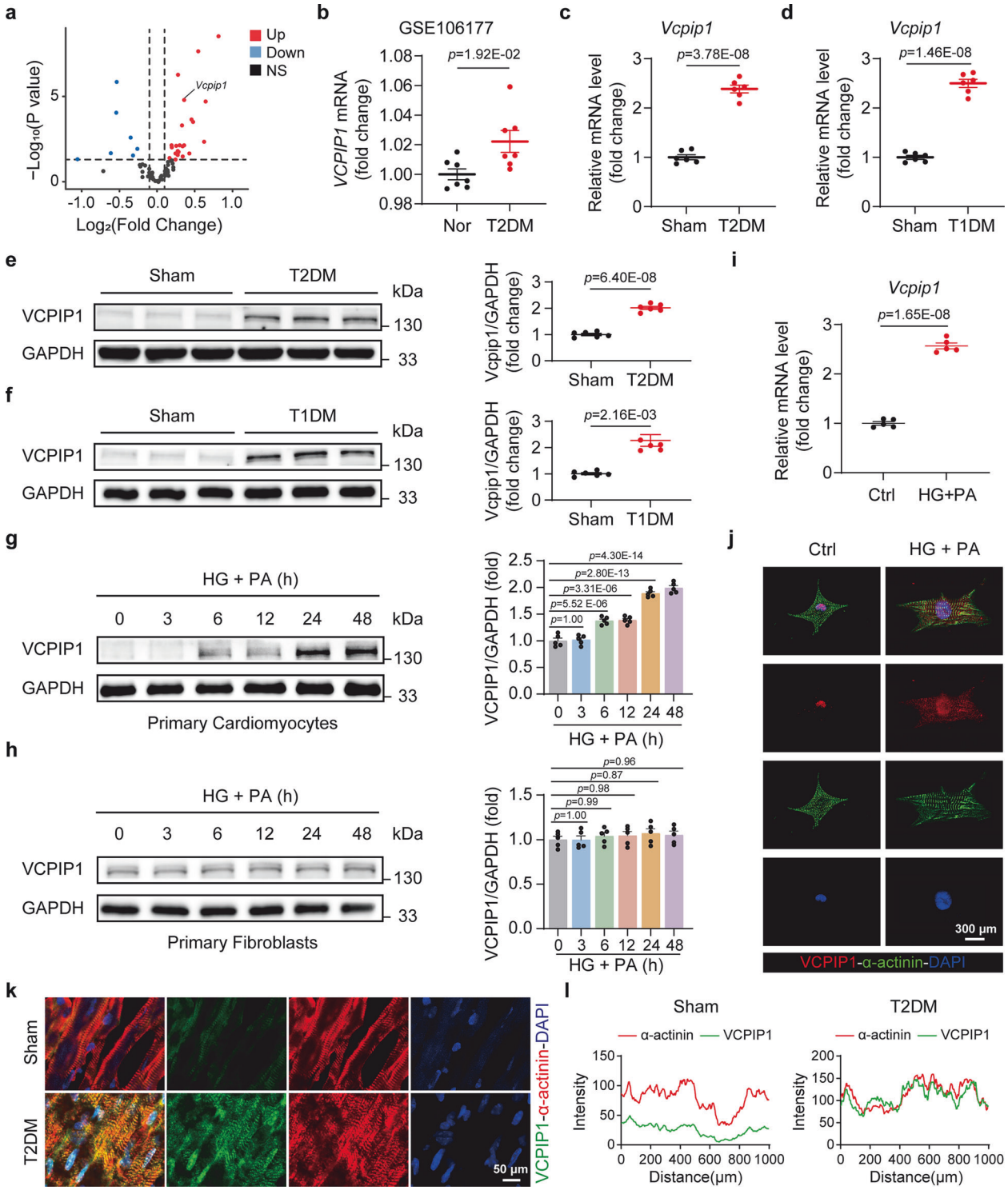

Fig. 1 Identification of cardiomyocyte-derived VCPIP1 involved in DCM progression. **a** RNA-seq data from the public dataset (GSE197999) were analyzed to profile deubiquitinating enzymes (DUBs), and the results were depicted as a volcano plot. **b** The mRNA levels of *VCPIP1* between normal individuals (Nor) and T2DM patients (T2DM) from a public dataset (GSE106177). **c**, **d** The mRNA levels of *Vcpip1* in the heart tissues from T2DM and T1DM mice. **e**, **f** Representative immunoblot and densitometric analysis of VCPIP1 in heart tissues from T2DM and T1DM mice. **g**, **h** Time-course of VCPIP1 protein expression in primary cardiomyocytes or primary fibroblasts exposed to high glucose (HG; 33 mM) and palmitic acid (PA; 100 μM) for indicated times (0, 12, 24, and 48 h). **i** The mRNA levels of *Vcpip1* in primary cardiomyocytes challenged with HG and PA for 24 h. **j** Representative images of immunofluorescence staining for VCPIP1 (red), α-actinin (green), and DAPI (blue) in primary cardiomyocytes with HG and PA stimulation for 24 h. **k**,**l** Immunofluorescence staining and fluorescence-intensity quantification of VCPIP1 (green), α-actinin (red), and DAPI (blue) in heart tissues from T2DM mice. For (**j**), scale bar = 300 μm; For (**k**), scale bar = 50 μm. Data are shown as mean ± SEM; **a**: $n = 5$; **b**: $n = 7$; (**c**–**f**), and (**k**,**l**): $n = 6$; (**g**–**j**): $n = 5$; For (**b**–**e**, **i**), *P* values were determined by Student *t* test; For **f**, *P* values were determined by Welch's *t* test; For (**g**, **h**), *P* values were determined by one-way ANOVA followed by Tukey post hoc tests; *P* values indicated

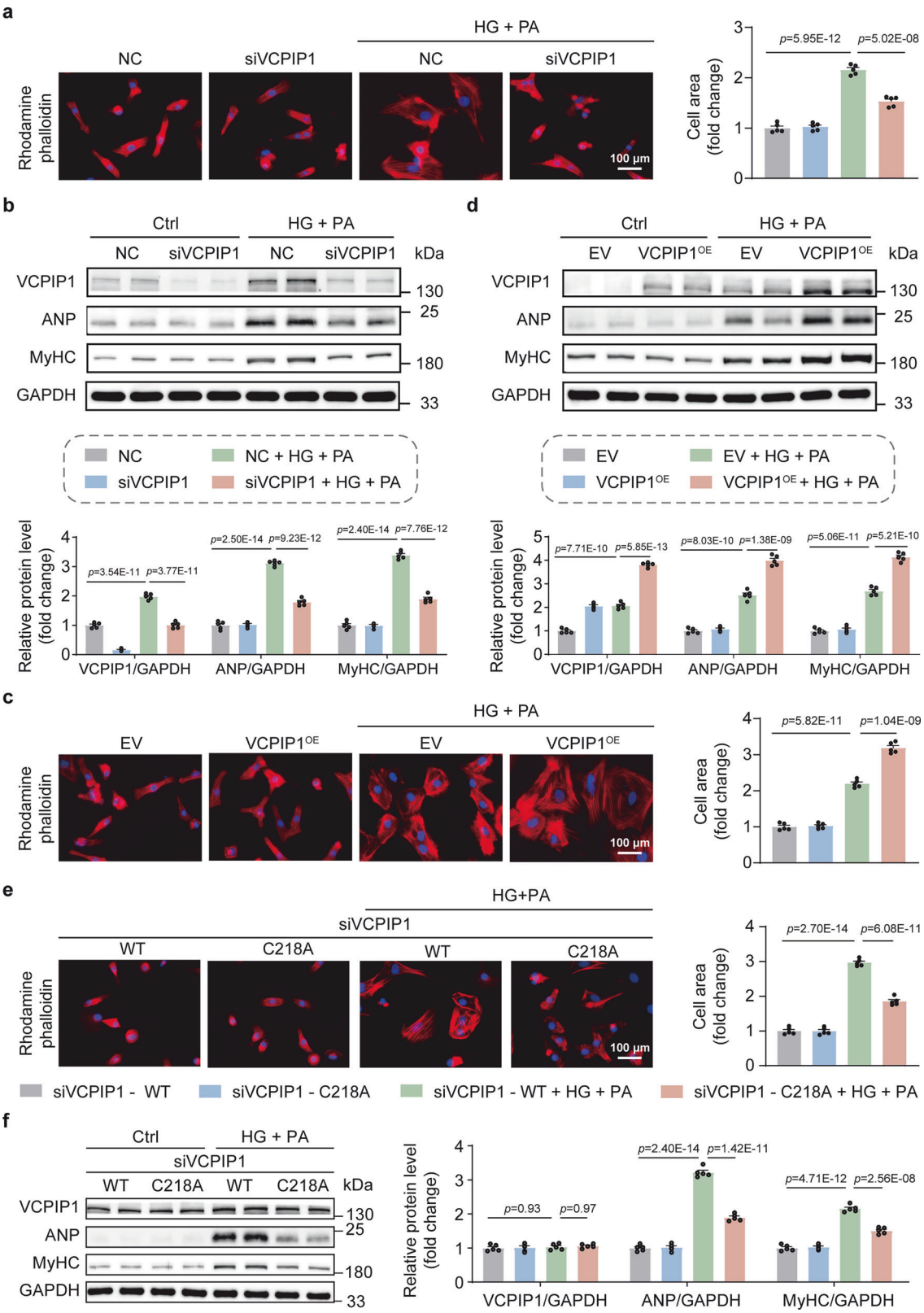

4a–e). The examinations on the cardiac fibrosis, such as positive areas of Masson's trichrome staining and Sirius red staining in heart tissues, showed VCPIP1 CKO significantly mitigated T1DM-induced fibrosis in mouse hearts (Supplementary Fig. 4f, g). Together, cardiomyocyte-specific VCPIP1 ablation also mitigates T1DM-induced cardiomyopathy.

AMPKγ1 is the deubiquitinated substrate of VCPIP1

Since VCPIP1 positively regulates hypertrophy via its deubiquitinating activity, we tried to identify the potential deubiquitinated substrates of VCPIP1 in cardiomyocytes. We performed both ubiquitinome and interactome analysis by immunoprecipitation and mass spectrometry assay in cardiomyocytes overexpressing

Fig. 2 VCPIP1 positively regulates hypertrophy in cardiomyocytes under diabetic condition. **a** Primary cardiomyocytes transfected with siRNA targeting VCPIP1 (siVCPIP1) or scrambled negative control (NC), and subsequently stimulated with high glucose (HG; 33 mM) and palmitic acid (PA; 100 μM) for 24 h. Representative images of rhodamine phalloidin staining and quantification of cell area were shown. **b** Western blot analysis VCPIP1, ANP, and MyHC in primary cardiomyocytes treated as indicated. **c** Primary cardiomyocytes were transfected with VCPIP1 plasmids ($VCPIP1^{OE}$), or empty vector (EV) were challenged with HG and PA for 24 h. Representative images of rhodamine phalloidin staining and quantification of cell area. **d** Western blot analysis and densitometric quantification of VCPIP1, ANP and MyHC. **e** Endogenous VCPIP1 was silenced with siVCPIP1, and primary cardiomyocytes were co-transfected with plasmid encoding either wild type VCPIP1 (WT) or mutation VCPIP1 of cysteine to alanine at C218 site (C218A). Cells were then treated with HG and PA for 24 h. Representative images of rhodamine phalloidin staining and quantification of cell area were presented. **f** Western blot and densitometric analyses of VCPIP1, ANP and MyHC. For (**a**, **c**, **e**), scale bar = 100 μm. Data are shown as mean ± SEM; $n = 5$; For (**a**–**d**), *P* values were determined by one-way ANOVA followed by Tukey post hoc tests; For (**e**, **f**), *P* values were determined by Student *t* test; *P* values indicated

VCPIP1 (Fig. 4a). The ubiquitinome analysis showed 103 proteins with downregulated ubiquitination (Flag-VCPIP1/Vector < 0.5) in cardiomyocytes transfected with Flag-VCPIP1, and the interactome analysis found 141 proteins potentially interacting with VCPIP1 in cardiomyocytes (Fig. 4a). Combining these two datasets, we identified 8 potentially deubiquitinated substrates of VCPIP1, including RNA terminal phosphorylase B (RTCB), AMPKγ1, eukaryotic translation initiation factor 3 subunit A (eIF3A), eukaryotic translation initiation factor 2α (eIF2α), transketolase (TKT), myosin VI (MYO6), USP5, and MCM protein 2 (MCM2; Fig. 4b). From this list, we excluded RTCB and MCM2 due to their lack of established relevance to cardiac pathophysiology.[26–31] To further prioritize the remaining candidates, we interrogated our previously generated single-cell RNA sequencing (scRNA-seq) dataset from mouse hearts[32] and found that *Tkt*, *Myo6*, and *Prkag1* (the gene encoding AMPKγ1) were highly expressed in cardiomyocytes (Supplementary Fig. 5a). We individually silenced TKT, MYO6, and AMPKγ1 using siRNA in HG + PA-challenged primary cardiomyocytes. Strikingly, only knockdown of AMPKγ1 abolished the anti-hypertrophic effect conferred by siVCPIP1 (Supplementary Fig. 5b). In addition, the roles of TKT and MYO6 in DCM are less defined. This analysis promotes us to choose AMPKγ1 as the functional substrate of VCPIP1 as the functional substrate of VCPIP1 for further investigation.

We then confirmed the interactions of VCPIP1 with AMPKγ1 in diabetic hearts and in HG + PA-challenged cardiomyocytes through Co-immunoprecipitation (Co-IP) assay (Fig. 4c, d and Supplementary Fig. 5c). Immunofluorescence staining also exhibited pronounced co-localization for VCPIP1-AMPKγ1 in primary cardiomyocytes upon HG + PA exposure (Fig. 4e, f). Notably, we performed proximity ligation assay (PLA) in H9C2 cells exposed to HG + PA to confirm the VCPIP1-AMPKγ1 interaction. As shown in Supplementary Fig. 6a, HG + PA treatment significantly enhanced the proximity signal between VCPIP1 and AMPKγ1, while siVCPIP1 markedly suppressed the signal of VCPIP1-AMPKγ1 interaction in cardiomyocytes. To evaluate the specificity of this interaction, we co-transfected Flag-tagged VCPIP1 with HA-tagged AMPK subunits (α2, β1, β2, and γ1) in HEK 293 T cells. Co-IP assays confirmed that VCPIP1 selectively interacted with the AMPKγ1 subunit (Supplementary Fig. 6b). A direct physical interaction between recombinant human VCPIP1 (rhVCPIP1) and rhAMPK proteins was confirmed by bio-layer interferometry (BLI) analysis, yielding a dissociation constant (KD) of 5.20×10^{-9} M (Fig. 4g). To map the molecular determinants governing VCPIP1-AMPKγ1 interaction, we engineered systematic truncation mutants of both proteins. As shown in Fig. 4h, VCPIP1 protein contains an OTU domain and a ubiquitin regulatory X-like (UBX-L) domain. AMPKγ1 could interact with the full-length Flag-VCPIP1 and the domain lacking Flag-OTU (Flag-$VCPIP1^{\Delta OTU}$), but not the domain lacking Flag-UBX-L (Flag-$VCPIP1^{\Delta UBX\text{-}L}$), indicating the UBX-L fragment of VCPIP1 protein as essential for this intermolecular association (Fig. 4i). Using the same methodology, we identified that VCPIP1 interacted with the CBS2 domain of AMPKγ1 (Fig. 4j, k). These results confirm that AMPKγ1 is the deubiquitinated substrate of VCPIP1 and the UBX-L domain of VCPIP1 directly binds to the CBS2 motif of AMPKγ1.

VCPIP1 deubiquitinates AMPKγ1 at K234 site, thereby limiting $AMPK^{T172}$ phosphorylation

We next explored the impacts of VCPIP1 on AMPK deubiquitination, stability, and activity in cardiomyocytes. We co-transfected Flag-VCPIP1, HA-AMPKγ1, and Myc-ubiquitin (Ub) in HEK 293 T cells, and found that VCPIP1 caused a marked decrease in AMPKγ1 ubiquitination (Fig. 5a). This trend was also seen in HG + PA-challenged primary cardiomyocytes and diabetic heart tissues (Supplementary Fig. 7a, b). In contrast, the inactive VCPIP1 induced by C218 mutant failed to remove the ubiquitin molecules from AMPKγ1 (Fig. 5b). Using site-specific ubiquitin variants (Myc-K48 or Myc-K63), we observed VCPIP1 preferentially cleaved K63-branched ubiquitin chains from AMPKγ1, whereas K48-linked chains remained unaffected upon VCPIP1 overexpression (Fig. 5c). In vivo, immunoprecipitation analysis of cardiac tissues from T2DM mice revealed that VCPIP1 CKO markedly depleted K63-linked ubiquitination, while leaving K48-linked ubiquitination unchanged (Supplementary Fig. 7c, d). As we know, K48-linked ubiquitinating modification mainly regulates protein stability, while K63 linkage prefers to regulate protein activity and function. Consistent with the deubiquitination linkage type, we found that VCPIP1 did not alter the protein levels of either AMPKγ1 or total-AMPK, but markedly suppressed AMPK activity, as indicated by the decreased AMPK phosphorylation at T172 site (Fig. 5d). VCPIP1 overexpression did not influence the mRNA levels of *PRKAA2* (encoding AMPKα2) or *PRKAG1* (encoding AMPKγ1; Supplementary Fig. 8a), consistent with post-translational regulation. Similarly, knockdown of VCPIP1 increased the phosphorylation levels of $AMPK^{T172}$ and acetyl-CoA carboxylase (ACC), while decreased the p-mTOR level in HG + PA-challenged primary cardiomyocytes (Fig. 5e and Supplementary Fig. 8b). Conversely, VCPIP1 overexpression decreased p^{T172}-AMPK and p-ACC levels, and increased p-mTOR, without altering total AMPK, ACC, and mTOR protein levels (Fig. 5f and Supplementary Fig. 8c). In vivo, cardiomyocyte VCPIP1 deficiency also upregulated p^{T172}-AMPK and p-ACC levels, along with downregulation of p-mTOR in T2DM mouse hearts (Fig. 5g and Supplementary Fig. 8d).

Given that AMPKγ1 is the predominant subunit in murine hearts, whereas AMPKγ2 is dominant in human hearts,[33,34] we validated the VCPIP1-AMPKγ2 regulatory axis in human AC16 cardiomyocyte line. Under HG + PA stimulation, the increased protein levels of ANP and MyHC in AC16 cells were significantly suppressed by VCPIP1 knockdown (Supplementary Fig. 9a, b). Knockdown of VCPIP1 also increased $AMPK^{T172}$ phosphorylation HG + PA-challenged AC16 cells without altering AMPKγ2 or total AMPK protein levels (Supplementary Fig. 9c, d). Notably, overexpression of VCPIP1 markedly reduced K63-linked polyubiquitination of AMPKγ2 in AC16 cells exposed to HG + PA (Supplementary Fig. 9e).

Our ubiquitinome analysis revealed 3 lysine residues of AMPKγ1 (K100, K234, and K264) appeared VCPIP1-mediated deubiquitination modification (Fig. 5h). We thus generated mutants of AMPKγ1 for these 3 sites (K100R, K234R, and K264R), and found that only K234R mutation abolished VCPIP1-mediated deubiquitination of AMPKγ1 (Fig. 5i), indicating that K234, an evolutionarily conserved residue (Supplementary Fig. 10a), as the critical site for VCPIP1-mediated deubiquitination of AMPKγ1. Ubiquitination of the

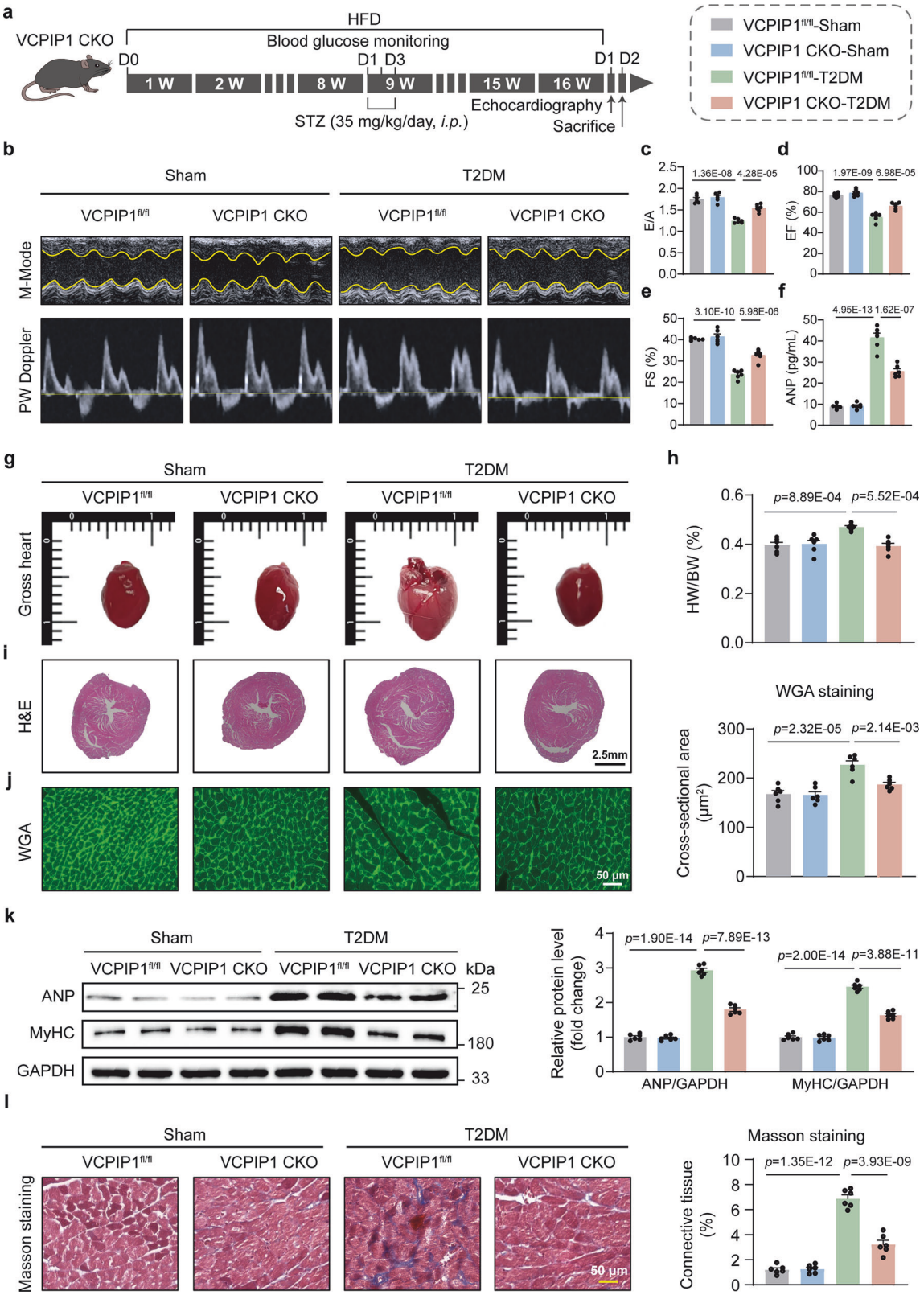

AMPKγ1 peptide containing K234 was shown in Supplementary Fig. 10b. To determine if K234 deubiquitination is responsible for the regulation of AMPK activity and cardiomyocyte hypertrophy, we generated AMPKγ1-deficient cardiomyocytes using CRISPR/Cas9 (Supplementary Fig. 10c), and then reconstituted them with either WT AMPKγ1 or the AMPKγ1-K234R. Compared to the WT AMPKγ1 group, K234R mutation, which represents K234 deubiquitination, diminished AMPK phosphorylation and elevated hypertrophic phenotypes in HG + PA-challenged cardiomyocytes (Fig. 5j, k). Under HG + PA stimulation, knockdown of VCPIP1

Fig. 3 Cardiomyocyte-specific VCPIP1 knockout alleviates cardiomyopathy in T2DM mice. **a** Schematic representation of the experimental design. VCPIP1$^{fl/fl}$ and VCPIP1 cardiomyocyte-specific knockout mice were induced to T2DM mice by low-dose streptozotocin (STZ, 35 mg/kg) administration for 3 days combining high-fat diet (HFD) feeding for 16 weeks. After 16 weeks, the cardiac function of the mice was evaluated, and blood samples along with heart tissues were harvested. **b** Representative pulse-wave (PW) Doppler and M-mode echocardiographic images in both VCPIP1$^{fl/fl}$ and VCPIP1 conditional knockout (CKO) groups. **c**–**e** Values of E to A peak velocity ratio (E/A), ejection fraction (EF%), and fractional shortening (FS%) by echocardiography. **f** Serum levels of atrial natriuretic peptide (ANP). **g** Representative images of whole heart. **h** The ratio of heart weight to body weight (HW/BW). **i** Representative images of H&E staining of transverse heart sections. **j** Wheat germ agglutinin (WGA) staining and quantification of cardiomyocyte area in heart tissues. **k** Western blot analysis and densitometric quantification of ANP and MyHC in heart tissues. **l** Representative images and quantification of Masson's Trichrome staining in heart tissues. For **i**, scale bar = 2.5 μm; For (**j**, **l**), scale bar = 50 μm. Data are shown as mean ± SEM; $n = 6$; P values were determined by one-way ANOVA followed by Tukey post hoc tests; P values indicated

enhanced AMPK phosphorylation and attenuated the hypertrophic phenotypes in cardiomyocytes with WT AMPKγ1 (Fig. 5j, k). However, in cardiomyocytes expressing the AMPKγ1-K234R, VCPIP1 knockdown failed to reduce the expression of hypertrophy-related genes (Fig. 5j, k). Collectively, these data indicate that VCPIP1 deubiquitinates AMPKγ1 at K234 site, thereby suppressing AMPK^{T172} phosphorylation to drive cardiomyocyte hypertrophic response.

VCPIP1-mediated AMPKγ1 deubiquitination disrupts the communication between AMPKα2 and γ1 to hinder AMPKα2-LKB1 interaction and AMPK^{T172} Phosphorylation

Then we tried to elucidate how VCPIP1-mediated AMPKγ1 deubiquitination limits AMPK^{T172} phosphorylation in cardiomyocytes. Previous structure studies on AMPK have indicated that AMPKα2 interacts with γ1 subunit and they form a complex to recruit the upstream kinase LKB1 for AMPKα2^{T172} phosphorylation in cardiomyocytes (Fig. 6a).[35,36] We assessed the possible effects of VCPIP1 on AMPKα2-γ1 interaction. Indeed, VCPIP1 overexpression limited the AMPKγ1-AMPKα2 interaction in HG + PA-induced cardiomyocytes and HEK 293 T cells (Fig. 6b, c). Notably, in HG + PA-challenged AMPKγ1-deficient cardiomyocytes, the K234R mutation diminished the AMPKα2-γ1 interaction, compared to the WT AMPKγ1 group (Fig. 6d). Additionally, AMPKα2 failed to interact directly with VCPIP1 in AMPKγ1-deficient cardiomyocytes (Fig. 6e). These data showed that VCPIP1-mediated AMPKγ1 deubiquitination hinders AMPKα2-γ1 interaction.

We further investigated whether VCPIP1-mediated AMPKγ1 deubiquitination affects AMPKα2-LKB1 interaction. As expected, overexpression of AMPKγ1 in AMPKγ1-deficient H9C2 cells rescued the binding between AMPKα2 and LKB1 under hyperglycemic condition (Fig. 6f), confirming that AMPKγ1 works as an essential scaffold for this interaction. Moreover, we found that overexpression of VCPIP1 reduced AMPKα2-LKB1 binding in both cardiomyocytes and HEK 293 T cells (Fig. 6g, h). These results suggest that VCPIP1-mediated AMPKγ1 deubiquitination induces an allosteric blockage against AMPKα2-γ1 inter-subunit communication, which subsequently limits LKB1 recruitment and LKB1-mediated AMPK^{T172} phosphorylation (Fig. 6i).

We further examined whether AMPK modulation can rescue or blunt the phenotypes induced by VCPIP1 manipulation in vitro. As shown in Supplementary Fig. 11a–c, AICAR treatment failed to attenuate the VCPIP1^{OE}-induced increase in cardiomyocyte surface area and the upregulation of hypertrophic markers. It suggests that VCPIP1 acts upstream to disrupt AMPK complex integrity, so that activating AMPK phosphorylation might not rescue the detrimental effect of VCPIP1. Conversely, the anti-hypertrophic effects of siVCPIP1 were completely blunted upon AMPK inhibition with compound C (CC) in HG + PA-stimulated cardiomyocytes (Supplementary Fig. 11d–f).

VCPIP1-mediated AMPKγ1 deubiquitination impairs cardiac mitochondrial OXPHOS in diabetic cardiomyocytes

Further, we explored how VCPIP1-mediated AMPKγ1 K234 deubiquitination and AMPK^{T172} dephosphorylation regulate hypertrophic response in cardiomyocytes. We performed a bulk RNA-sequencing analysis using HG + PA-challenged H9C2 cells with WT AMPKγ1 or AMPKγ1-K234R mutation, respectively. Principal component analysis revealed treatment-driven clustering (Fig. 7a). Compared to AMPKγ1-K234R^{OE} group, AMPKγ1^{OE} group exhibited 1850 upregulated and 2005 downregulated differentially expressed genes (DEGs; $|Log2FC| > 1$ and P value < 0.05; Fig. 7b). Analysis of upregulated DEGs via Gene Ontology (GO), specifically for cellular component (CC) and biological process (BP), highlighted the involvement of mitochondrion-related OXPHOS in AMPKγ1-regulated pathways (Fig. 7c). Consistent with this, GO enrichment and Gene Set Enrichment Analysis (GSEA) visualized that the mitochondrial respiratory chain complex and mitochondrial respirasome were mainly involved (Fig. 7d, e). Heat map further highlighted that mitochondrial respirasome-related DEGs were upregulated by AMPKγ1 in HG + PA-challenged H9C2 cells (Fig. 7f). In addition, immunofluorescence staining using the mitochondrial marker protein TOM20 revealed co-localization of VCPIP1 and AMPKγ1 with mitochondria in HG + PA-stimulated H9C2 cells (Supplementary Fig. 12a). These analyses indicate that VCPIP1-mediated AMPKγ1-K234 deubiquitination induces mitochondrial homeostasis disruption in cardiomyocytes.

Assessment of mitochondrial respiratory chain complexes revealed significantly decreased protein expression of complex I, III, and IV in both T2DM and T1DM murine hearts, while cardiomyocyte-specific VCPIP1 deficiency restored complex III and IV expression (Fig. 7g and Supplementary Fig. 12b, c). Similarly, HG + PA-challenged neonatal rat primary cardiomyocytes (NRPCs) exhibited significantly reduced expression of mitochondrial respiratory chain complex III and IV, a reduction that was effectively reversed by VCPIP1 silencing (Fig. 7h and Supplementary Fig. 12d). As expected, VCPIP1 overexpression exacerbated the decline in complex III and IV expression under HG + PA stimulation (Supplementary Fig. 12e). Protein expression of complex II and V remained unaltered throughout interventions. Mitochondrial function was next determined in NRPCs. The results showed that HG + PA significantly impaired complex I and II-mediated respiration and reduced the content of ATP in NRPCs, while VCPIP1 knockdown restored mitochondrial oxygen consumption and ATP production (Fig. 7i, j). VCPIP1 overexpression exacerbated mitochondrial dysfunction in HG + PA-treated cardiomyocytes (Supplementary Fig. 13a, b). Ultrastructural analysis revealed mitochondrial swelling, cristae loss, and reduced morphology scores in diabetic hearts, while VCPIP1 CKO attenuated these pathological changes (Fig. 7k). Consistent with these in vivo results, silencing VCPIP1 conferred analogous mitochondrial protection in HG + PA-challenged NRPCs, whereas VCPIP1 overexpression worsened the ultrastructural damage (Fig. 7l and Supplementary Fig. 13c–e). As a result of mitochondrial injury, HG + PA stimulation induced marked mitochondrial ROS generation in NRPCs, an effect that was abrogated by VCPIP1 knockdown (Fig. 7m). By contrast, VCPIP1 overexpression exacerbated ROS generation (Supplementary Fig. 13f).

We validated the functional impact of VCPIP1 in adult mouse primary cardiomyocytes (AMPCs). Immunostaining for α-actinin

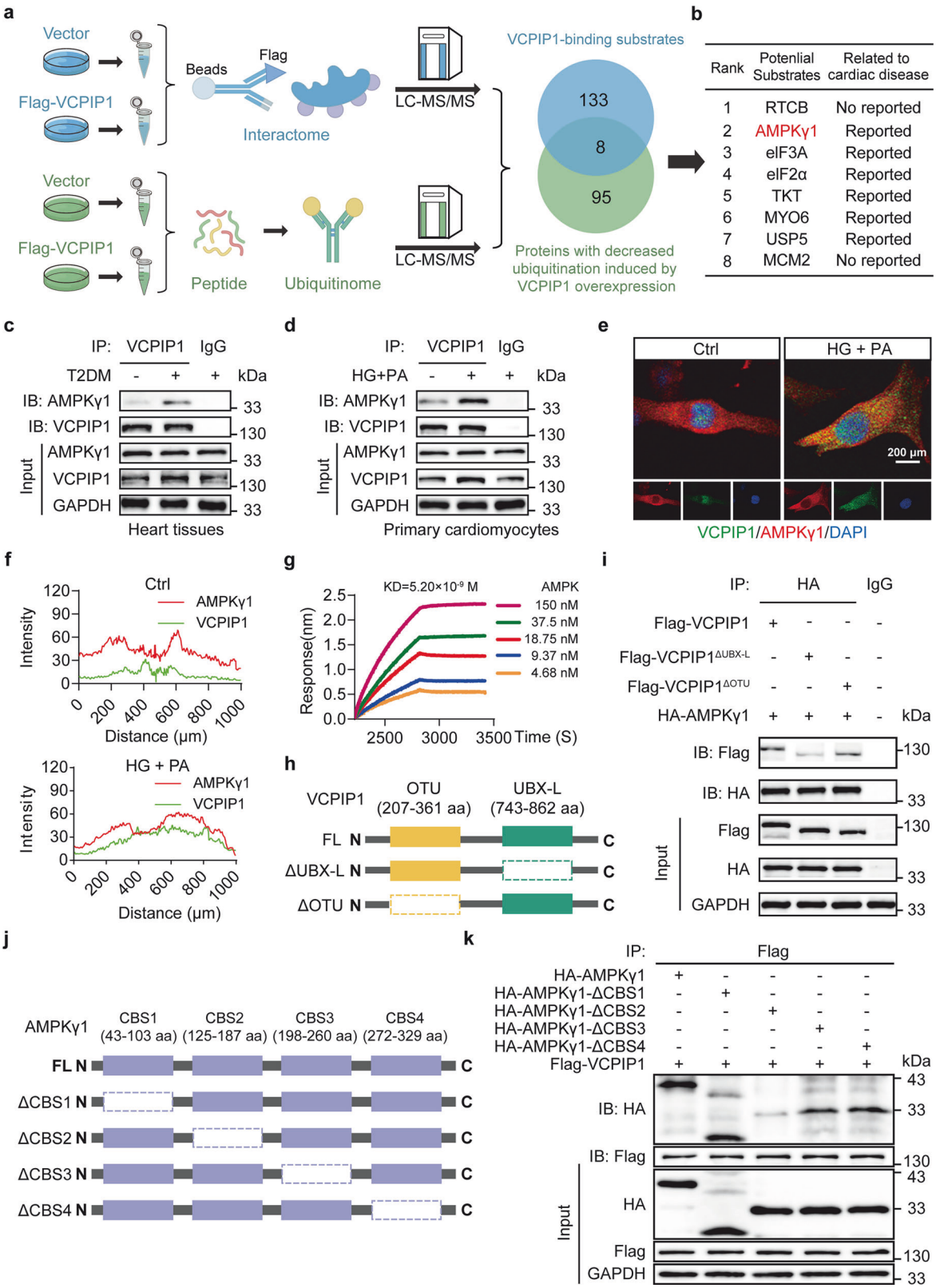

confirmed characteristic sarcomeric striations, verifying cardiomyocyte identity and structural integrity (Supplementary Fig. 14a). Under HG + PA stimulation, VCPIP1 knockdown significantly attenuated the upregulation of the pathological hypertrophy markers ANP and MyHC in AMPCs (Supplementary Fig. 14b). Furthermore, silencing VCPIP1 enhanced AMPK^{T172} phosphorylation and restored the protein expression of complexes III and IV, which were suppressed by HG + PA challenge (Supplementary Fig. 14c). Functionally, VCPIP1 knockdown rescued both mitochondrial oxygen consumption and ATP production in AMPCs (Supplementary Fig. 14d, e). These findings indicate that VCPIP1-mediated AMPKγ1 deubiquitination impairs mitochondrial homeostasis in diabetic cardiomyocytes.

Fig. 4 AMPKγ1 is the deubiquitinated substrate of VCPIP1. **a** Schematic of a comprehensive combined ubiquitinome and interactome analysis for VCPIP1 substrate screening. **b** Table for the eight candidate substrates of VCPIP1 that were screened. **c, d** Co-immunoprecipitation (Co-IP) of the interaction between VCPIP1 and AMPKγ1 in heart tissues from T2DM mice and in primary cardiomyocytes treated with HG and PA. **e, f** Representative immunofluorescence images and intensity quantification of VCPIP1 (green) and AMPKγ1 (red) in primary cardiomyocytes challenged with HG and PA. **g** Bio-layer interferometry (BLI) assay was used to detect VCPIP1 and AMPK binding, with AMPK titrated from 4.68 nM to 150 nM, and dissociation constant (KD) values were calculated. **h** Schematic diagram of truncated mutants of VCPIP1. **i** Co-IP between AMPKγ1 and VCPIP1 or mutants-VCPIP1 in HEK 293 T cells. **j** Illustration of the AMPKγ1 domain deletion construct, and co-IP of VCPIP1 with wild type-AMPKγ1 or mutants-AMPKγ1 (ΔCBS1, ΔCBS2, ΔCBS3, ΔCBS4) in HEK 293 T cells. **k** Co-IP between VCPIP1 and AMPKγ1 or mutants-AMPKγ1 in HEK 293 T cells. For **e**, scale bar = 200 μm. **c**–**k**: $n = 5$

AMPKγ1-K234R mutation phenocopies VCPIP1-mediated DCM in *db/db* mice

We further validated the positive regulation of VCPIP1-mediated AMPKγ1 K234 deubiquitination on diabetic cardiomyopathy in mice. We generated recombinant Adeno-Associated Virus 9 (AAV9) vectors carrying WT AMPKγ1 ($AMPK\gamma1^{OE}$), AMPKγ1-K234R mutation ($AMPK\gamma1^{K234R}$), and VCPIP1 ($VCPIP1^{OE}$). These AAVs were delivered via tail vein injection to *db/db* mice, with blood glucose monitored two weeks later (Fig. 8a). As anticipated, neither $AMPK\gamma1^{OE}$ nor $AMPK\gamma1^{K234R}$ altered systemic metabolic parameters, including hyperglycemia, serum insulin, total cholesterol, or triglyceride levels in *db/db* mice (Supplementary Fig. 15a and Table 3). Critically, $VCPIP1^{OE}$ abrogated $AMPK\gamma1^{OE}$-induced cardioprotection effects including improvements in cardiac function, the increased ANP levels, hypertrophy, and fibrosis in *db/db* mice (Fig. 8b–j, and Supplementary Fig. 15d, e and Table 3). Compared to the AAV9-$AMPK\gamma1^{OE}$ group, overexpression of AMPKγ1-K234R mutation in AAV9-$AMPK\gamma1^{K234R}$ group failed to reverse diabetic heart injuries in *db/db* mice (Fig. 8b–j, Supplementary Fig. 15b, c and Table 3). Notably, $VCPIP1^{OE}$ failed to further deteriorate cardiac function and hypertrophy in *db/db* mice when cardiomyocytes existed AMPKγ1-K234R mutation (Fig. 8b–j, Supplementary Fig. 15b, c and Table 3), indicating functional dependence on K234 ubiquitination. Consistently, $VCPIP1^{OE}$ decreased the levels of complex III and IV in $AMPK\gamma1^{OE}$ diabetic heart tissues, but not in $AMPK\gamma1^{K234R}$ heart tissues (Fig. 8k). Collectively, these results establish that AMPKγ1-K234 deubiquitination is critically responsible for the VCPIP1 mediated cardiac pathology in DCM.

DISCUSSION

The functional interplay between deubiquitinating modification and mitochondrial dysfunction underlying DCM development remains poorly characterized. Our work delineates cardiomyocytes VCPIP1 as a new modulator of AMPK activity and mitochondrial integrity in DCM. Both diabetic myocardial tissues and HG + PA-stimulated cardiomyocytes showed increased VCPIP1 expression. Genetic ablation of *Vcpip1* in cardiomyocytes rescued cardiac dysfunction and hypertrophy in both T1DM and T2DM mouse models. Mechanistically, VCPIP1 directly binds to AMPKγ1 via its catalytic residue C218, catalyzing K63-linked deubiquitination at AMPKγ1 K234 site. Interestingly, the VCPIP1-mediated AMPKγ1 deubiquitination damages AMPKα2-γ1 subunit communication and then disrupts AMPKα2-LKB1 interaction via allosteric regulation, limiting the phosphorylation of $AMPK^{T172}$. The AMPKγ1-K234R mutant phenocopied VCPIP1-mediated cardiac hypertrophy in *db/db* mice. Transcriptomic profiling further established that VCPIP1-AMPK axis induces mitochondrial dysfunction in cardiomyopathy and drives DCM development. These findings present a new VCPIP1-AMPK axis and nominate VCPIP1 as a key node for DCM treatment, with key mechanisms summarized in the Graphical Abstract.

DUBs have been reported to modulate cardiomyocyte pathophysiology under diverse pathological conditions, including hyperglycemia, hypertension, obesity, and external endotoxin stimuli.[37–40] Our research team has explored cardioprotective DUBs networks, delineating USP25 and JOSD2 as stabilizers of SERCA2a that preserve calcium homeostasis against hypertensive and pressure overload-induced cardiac hypertrophy.[19,41] However, the DUB landscape in DCM remains rarely characterized. Recent study reported that cardiac-specific knockout of USP28 aggravated DCM progress via deubiquitinating and stabilizing peroxisome proliferator-activated receptor α (PPARα).[21] Contrarily, USP7 knockdown ameliorated morphological and functional impairments in diabetic hearts through stabilization of peroxisome proliferator-activated receptor gamma coactivator 1-beta.[42] Our study uncovered VCPIP1 as a novel pathogenic DUB in diabetic hearts. We revealed pathological upregulation of cardiomyocyte VCPIP1 in experimental DCM models. Previously, VCPIP1 functioned as an oncogenic deubiquitinase and the clinical analyses confirmed its elevation in pancreatic adenocarcinoma correlates with poor patient survival.[24] VCPIP1 also stabilized MATIIα in hepatocellular carcinoma under folate stress[43] and impeded neuronal recovery by blocking botulinum toxin degradation,[44] highlighting its multifaceted pathological roles. Our findings implicate VCPIP1 in cardiomyocytes as a driver of DCM pathology, positioning this DUB as a viable target for therapeutic intervention.

DUBs exert their regulatory functions primarily via deubiquitinating the specific substrate proteins.[18] It has been reported that VCPIP1 deubiquitinates context-dependent substrates including YAP,[24] Erbin,[45] and HBV[22] in distinct pathologies. Our work reveals AMPKγ1 as a bona fide substrate of VCPIP1 in hypertrophic cardiomyocytes. Notably, sustained hyperglycemia suppresses cardiac AMPK activity during advanced DCM stages, concomitant with irreversible myocardial damage; conversely, therapeutic maintenance of AMPK activation alleviates DCM[12,13] and represents an effective intervention strategy against DCM. Our data also showed that AMPK K234R mutant phenocopied VCPIP1-mediated cardiac hypertrophy in diabetic mice, validating that AMPK is a functionally relevant substrate through which VCPIP1 promotes DCM pathogenesis in cardiomyocytes.

As a regulatory subunit of the AMPK heterotrimer, AMPKγ1 contains four CBS domains, with CBS1/3/4 binding nucleotide, such as ATP.[46] This enables AMPKγ1 to sense declining ATP levels, triggering $AMPK\alpha^{T172}$ phosphorylation via AMPKα-γ interunit communication to maintain cellular energy homeostasis.[47] Although AMP-mimetics like ZMP activate AMPK via γ subunit nucleotide-binding sites, the non-selective effects on AMP-sensitive enzymes (e.g., fructose-1,6-bisphosphatase) limit their therapeutic utility.[47] We demonstrated that VCPIP1 binds to the CBS2 domain, a non-nucleotide-binding region of AMPKγ1, to mediate its deubiquitination. VCPIP1 removes K63-linked ubiquitin chains from AMPKγ1 to negatively regulate AMPK activity. Inhibition of VCPIP1 elevated the levels of p^{T172}-AMPKα in hyperglycemic cardiomyocytes and cardiac tissues, establishing a non-canonical AMPK activation strategy that bypasses the metabolic sensor limitation. AMPKγ1 is predominantly expressed in murine hearts, whereas AMPKγ2 dominates in human hearts (AMPKγ3 negligible).[33,34] Supporting translational relevance, we found that VCPIP1 also binds to and deubiquitinates AMPKγ2 to downregulate AMPK phosphorylation in human cardiomyocytes under diabetic condition.

It's unsurprising that the stability and enzymatic activity of AMPK are governed by multiple PTMs types, spanning

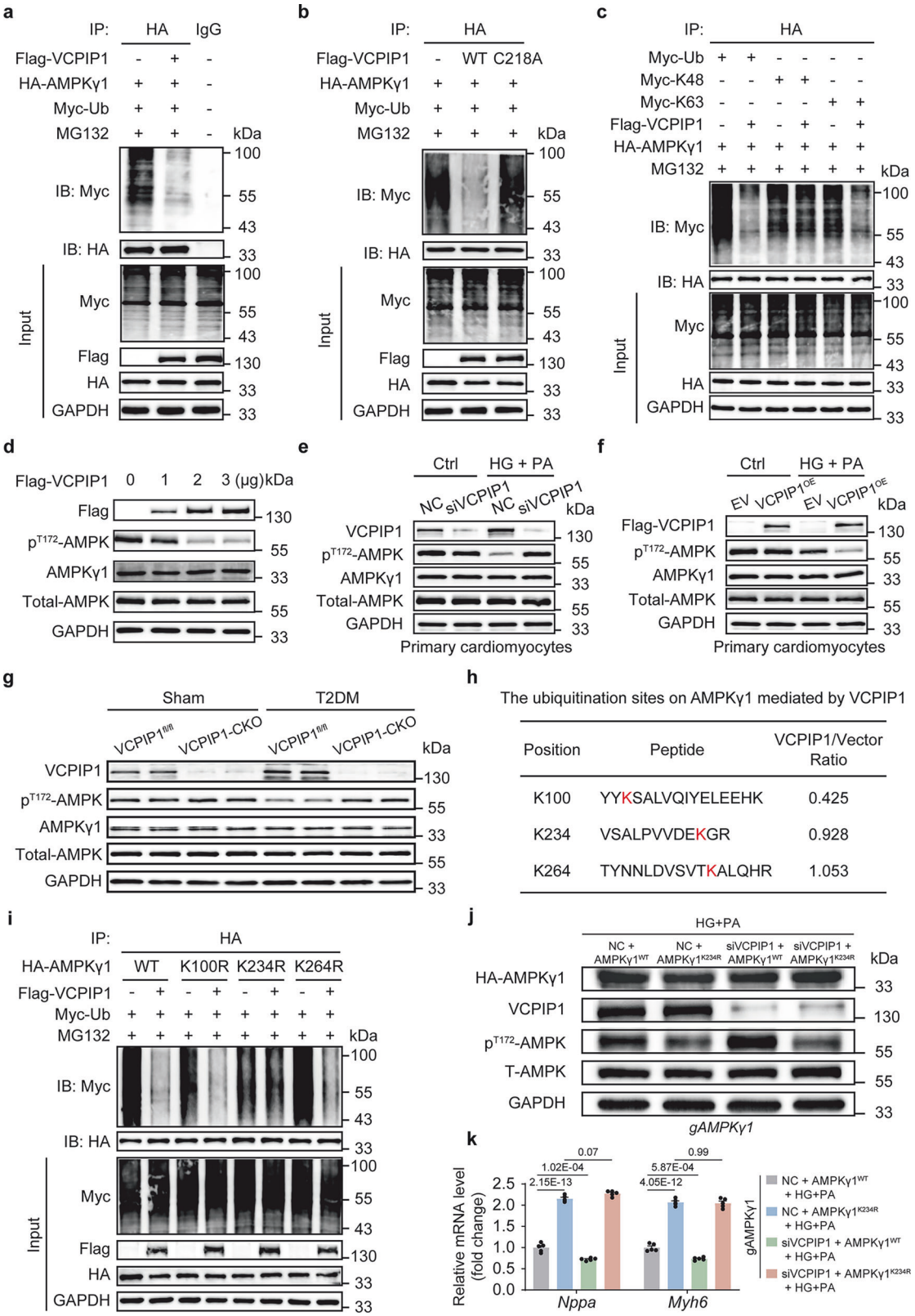

phosphorylation, ubiquitination, SUMOylation, acetylation, and methylation.[48–51] Especially, the phosphorylation of AMPK at Thr172 directly represents the activated situation of AMPK, and other modifications regulate AMPK activity through indirectly affecting AMPK^{T172} phosphorylation.[51] Evidence indicates that WWP1, an E3 ubiquitin ligase containing WW domains, promotes AMPKα2 proteasomal degradation.[52] Also, CIDEA regulates β1-subunit protein stability through polyubiquitination.[53] Our research and others have reported that AMPK ubiquitination can also exert non-degradative effects on AMPK activity. For example, OTUD1 deubiquitinases its substrates by trimming K63-linked polyubiquitin moieties from AMPKα to limit AMPKα^{T172}

Fig. 5 VCPIP1 deubiquitinates AMPKγ1 at K234 site, thereby limiting AMPK^{T172} phosphorylation. **a** HEK 293 T cells were co-transfected with HA-AMPKγ1, Flag-VCPIP1, and Myc-ubiquitin (Myc-Ub) plasmids, followed by treatment with 10 μM MG132 for 6 h. Ubiquitinated AMPKγ1 was detected via immunoblotting. **b** HEK 293 T cells were co-transfected with Myc-Ub, HA- AMPKγ1, Flag-VCPIP1-WT or Flag-VCPIP1-C218A plasmids. Ubiquitinated AMPKγ1 was detected by immunoblotting. **c** Co-immunoprecipitation (Co-IP) assay demonstrated the ubiquitination of AMPKγ1 by K48-Ub or K63-Ub in HEK 293 T cells. **d** Western blot analysis of phosphorylated AMPK (p^{T172}-AMPK), Total AMPK, and AMPKγ1 in HEK 293 T cells transfected with Flag-VCPIP1 plasmids in indicated dose (1, 2, and 3 μg). **e**, **f** Primary cardiomyocytes were transfected with siRNA targeting VCPIP1 (siVCPIP1), scrambled negative control (NC), VCPIP1 plasmids (VCPIP1^{OE}), or empty vector (EV) for 24 h. The protein levels of p^{T172}-AMPK, Total AMPK, and AMPKγ1 were detected via immunoblotting. **g** Western blot analysis of p^{T172}-AMPK, Total AMPK, and AMPKγ1 in heart tissues from sham and T2DM mice in both VCPIP1$^{fl/fl}$ and VCPIP1 conditional knockout (CKO) groups. **h** Ubiquitinome analysis identified three lysine residues (K100, K234, and K264) on AMPKγ1 appeared deubiquitylation modification by VCPIP1. **i** Co-IP assay was performed in HEK 293 T cells co-transfected with Myc-Ub, HA-AMPKγ1, or mutants AMPKγ1 (K100R, K234R, or K264R) plasmids. Ubiquitinated AMPKγ1 was detected by immunoblotting. **j** AMPKγ1-deficient H9C2 cells were transfected with siVCPIP1, NC, HA-AMPKγ1-WT, and HA-AMPKγ1-K234R plasmids, and then exposed to high glucose (HG; 33 mM) and palmitic acid (PA; 100 μM). The expressions of p^{T172}-AMPK and Total AMPK were detected. **k** RT-qPCR analysis of hypertrophic genes. Data are shown as mean ± SEM; $n = 5$; P values were determined by Student t test; P values indicated

phosphorylation in cardiomyocytes.[54] In contrary, another DUB, USP10, deubiquitinates AMPKα to facilitate AMPKα phosphorylation by LKB1, increasing AMPK activity.[48]

However, previous studies on ubiquitination/deubiquitination of AMPK focused on the α- and β-subunits, largely neglecting γ-subunit modifications. In fact, AMPKγ is very important as it acts as an essential scaffold for AMPK assembly. Our data reported the deubiquitination modification of AMPKγ1 at the first time. We further showed that VCPIP1-mediated deubiquitination of AMPKγ1 at K234 negatively regulates AMPKα^{T172} phosphorylation. This regulatory paradigm operates through disruption of inter-subunit communication, which is a prerequisite for AMPK assembly and activation. Structural studies demonstrate that AMPK's conformational switch requires coordinated interactions between the AID/α-linker of α-subunit and the nucleotide-binding sites of γ-subunit, enabling allosteric regulation for LKB1 recruitment and AMPKα^{T172} phosphorylation.[36,54] Interestingly, we reveal that VCPIP1 disrupts AMPKα2-γ1 complex formation via deubiquitinating AMPKγ1, thereby diminishing LKB1 recruitment and AMPKα^{T172} phosphorylation in cardiomyocytes. Importantly, we found AMPKγ1 acts as an essential scaffold for this kinase-substrate recognition. Here, we reveal a distinct regulatory mechanism through which deubiquitination of AMPKγ1 regulates AMPKα^{T172} phosphorylation and activity.

Previous reviews summarize that AMPK activation protects cardiomyocytes from pathological injury by modulating multiple downstream pathways, including regulating mitochondrial function.[55,56] Our RNA-seq data implicate VCPIP1-mediated deubiquitination of AMPKγ1-K234 related to mitochondrial dysfunction in cardiomyocytes. Small molecule AMPK activators (e.g., metformin, AICAR, melatonin) mitigate cardiac injury via mitochondrial modulation in animal models.[13,55,56] While our prior work established that PRL2 drives pathological cardiac hypertrophy by suppressing mitochondrial oxidative phosphorylation through AMPKα^{T172} dephosphorylation.[12] The current study reveals a novel ubiquitin-dependent pathway governing this axis. Consistent with this, hyperglycemia-challenged cardiomyocytes and cardiac tissues exhibited profound suppression of OXPHOS, structural mitochondrial abnormalities, and excessive ROS accumulation, all of which were reversed by VCPIP1 deficiency in cardiomyocytes. Thus, the VCPIP1-AMPKγ1 axis orchestrates mitochondrial bioenergetics in cardiomyocytes, representing a fundamental pathogenic mechanism in DCM progression. Notably, the effect of VCPIP1 overexpression was minimal under basal conditions but pronounced in diabetic settings, consistent with the context-dependent increase in K63-linked ubiquitination of AMPKγ1 under diabetic environment, highlighting that VCPIP1 is a pathological target and targeting VCPIP1 may be of high safety in healthy subjects.

In summary, our work establishes a novel VCPIP1-AMPK regulatory axis that governs mitochondrial bioenergetics in DCM. We reveal that VCPIP1 binds to and deubiquitinates AMPKγ1 at K234, disrupting the integrity of the AMPKα/γ heterodimer and suppressing LKB1 recruitment and LKB1-mediated AMPKα^{T172} phosphorylation. These findings delineate a non-canonical mechanism for AMPK activation in cardiomyocytes, suggesting that targeting VCPIP1 by small-molecule inhibitors, represents a novel therapeutic strategy to activate AMPK in DCM. Since mitochondrial dysfunction and impaired AMPK signaling are common across other cardiac pathologies, further investigation is warranted to explore the relevance of VCPIP1 in a broader spectrum of heart diseases.

MATERIALS AND METHODS

Mice

The male C57BL/6 J mice (8 weeks, weight 20-22 g) and the *db/db* mice (8 weeks, weight 40–42 g) were procured from the Laboratory Animal Center of Hangzhou Medical College (Hangzhou, China). The animals resided in drafty cages within a specific pathogen-free (SPF) facility. Male C57BL/6J-*Vcpip1*^{em1Cflox} (*VCPIP1*$^{fl/fl}$, strain No. T064955) mice and C57BL/6J-*H11*$^{em1Cin(Myh6\text{-}CreERT2)}$ (*Myh6*-CreERT2, strain No. T060079) mice were bought from GemPharmatech (Nanjing, China). The cardiac-specific *VCPIP1*-knockout (*VCPIP1*$^{fl/fl}$+*Myh6*-CreERT2$^{+/-}$, *VCPIP1*-CKO) mice were generated by crossing *VCPIP1*$^{fl/fl}$ mice with *Myh6*-Cre^{ERT2} mice. All experimental procedures were conducted in accordance with the National Institutes of Health Guidelines for the Care and Use of Laboratory Animals. All study procedures were approved by the Ethics Committee of Laboratory Animal Care and Welfare, Hangzhou Medical College (Approval Number: ZJCLA-IACUC-20010339).

Sample size and blinding procedures in vivo

For in vivo experiments, the sample size was calculated utilizing G-Power software with a two-tailed α of 0.05, a statistical power of 80%, and an effect size of 0.8. This effect size was estimated based on preliminary results of serum ANP levels and ejection fraction measurements. According to this power analysis, at least 6 mice per group was essential. All animal studies adhered to this estimate, with 6 mice included in each experimental group. Data acquisition and assessment were carried out independently by two researchers who remained unaware of group allocation and animal phenotypes.

Animal experiments

T1DM model: *VCPIP1*-CKO mice along with their *VCPIP1*$^{fl/fl}$ littermates were allocated into four groups: *VCPIP1*$^{fl/fl}$-Sham group, *VCPIP1*-CKO-Sham group, *VCPIP1*$^{fl/fl}$-T1DM group, and *VCPIP1*-CKO-T1DM group. Mice were administered STZ (60 mg/kg, *i.p.*; dissolved in citrate buffer; Sigma-Aldrich, St Louis, MO, USA) over three successive days. Fasting blood glucose (FBG) was monitored every two weeks using a glucometer. Successful diabetic induction was confirmed when animals exhibited FBG levels ≥ 12 mmol/L on two sequential measurements, qualifying them for downstream analyses.

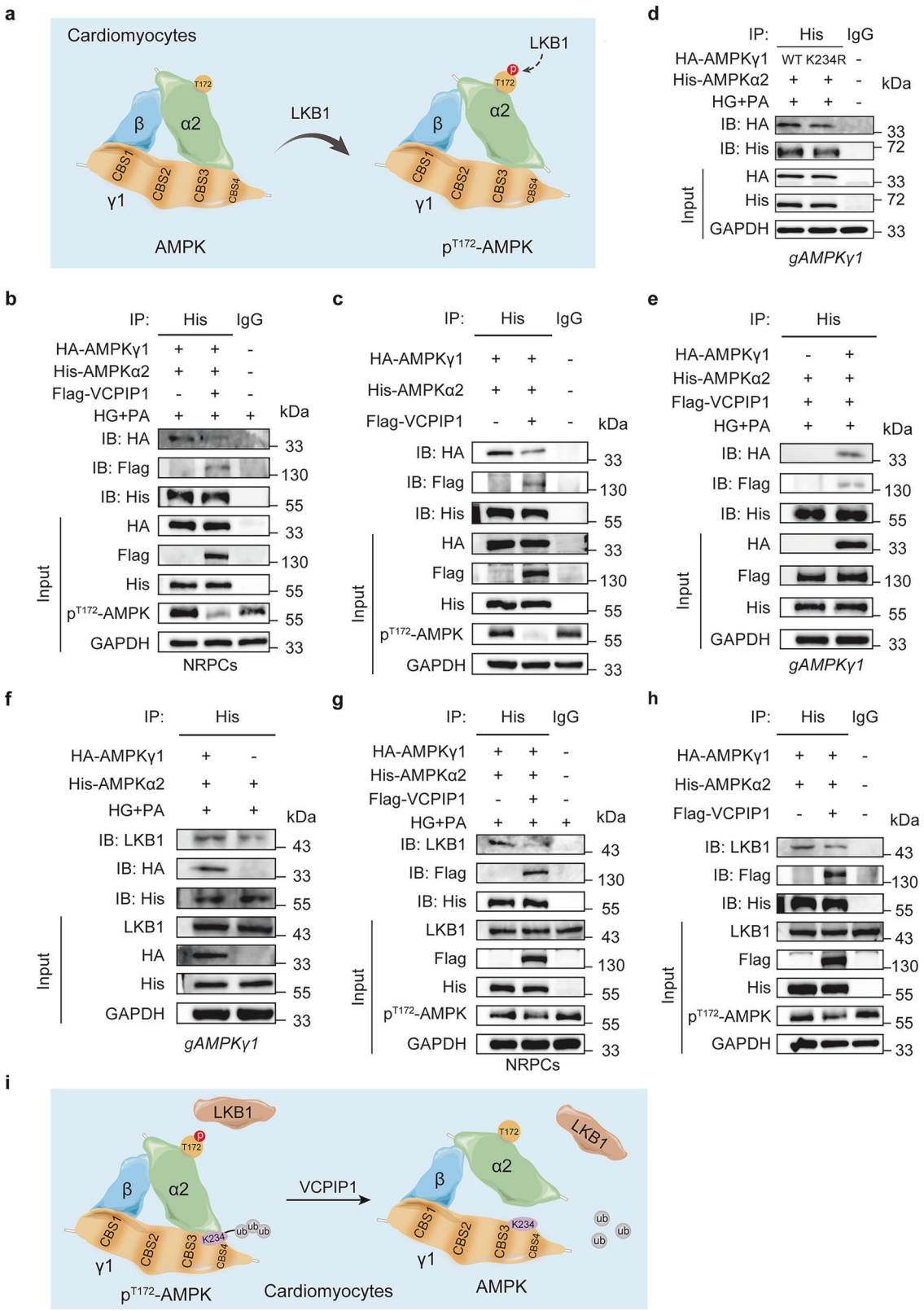

T2DM model: *VCPIP1*-CKO mice along with their *VCPIP1*$^{fl/fl}$ littermates were equivalently distributed among four groups: *VCPIP1*$^{fl/fl}$-Sham group, *VCPIP1*-CKO-Sham group, *VCPIP1*$^{fl/fl}$-T2DM group, and *VCPIP1*-CKO-T2DM group. The mice were fed either a HFD (60.3 kcal% fat; D12492I, New Brunswick, NJ, USA) or standard chow for 16 weeks. After the initial 8 weeks of the HFD regimen, low-dose STZ (35 mg/kg) was administered intraperitoneally over three successive days. Upon completion of the 16-week experimental timeline, mice were anesthetized with intraperitoneal pentobarbital sodium (40 mg/kg), followed by sacrifice via cervical

Fig. 6 VCPIP1-mediated AMPKγ1 deubiquitination disrupts the communication between AMPKα2 and γ1 to hinder AMPKα2-LKB1 interaction and $AMPK^{T172}$ Phosphorylation. **a** Schematic representation for the potential molecular mechanism of reduction in $AMPK^{T172}$ phosphorylation. **b**, **c** Primary cardiomyocytes and HEK 293 T cells were co-transfected with HA-AMPKγ1, His-AMPKα2, Flag-VCPIP1 plasmids. The interaction between AMPKγ1 and AMPKα2, and the levels of p^{T172}-AMPK were detected. **d** AMPKγ1-deficient H9C2 cells were co-transfected with HA-AMPKγ1-WT, HA-AMPKγ1-K234R, and His-AMPKα2 plasmids, and the AMPKγ1-AMPKα2 binding was evaluated by Co-IP. **e** Co-immunoprecipitation (Co-IP) examined the AMPKα2–VCPIP1 interaction in AMPKγ1-deficient H9C2 cells overexpression AMPKγ1, AMPKα2 and VCPIP1. **f** The interaction between AMPKα2 and LKB1 in AMPKγ1-deficient H9C2 cells overexpression AMPKγ1 and AMPKα2. **g**, **h** Co-IP assay of AMPKα2-LKB1 interaction, and immunoblotting of p^{T172}-AMPK in both primary cardiomyocytes and HEK 293 T cells treated as indicated. **i** Schematic representation of VCPIP1 drives the reduction in $AMPK^{T172}$ phosphorylation. $n = 5$

dislocation. Cardiac tissues were rapidly excised, weighed, and collected. Concurrently, blood was drawn and centrifuged to obtain serum, which was used for ANP analysis by the ELISA kit (E-EL-M0166, Elabscience, Wuhan, China).

AAV9 Infection

To overexpress AMPKγ1, $AMPK\gamma1^{K234R}$, and VCPIP1 in vivo, male *db/db* mice were treated with rAAV9 vectors harboring the coding sequences of these genes under the control of *cTnT* promoter (rAAV9-*cTnT-AMPKγ1* and rAAV9-*cTnT-*$AMPK\gamma1^{K234R}$). The *AMPKγ1*, $AMPK\gamma1^{K234R}$, and *VCPIP1* genes were cloned into rAAV9 by Genechem Co. LTD (Shanghai, China). The *db/db* mice anesthetized with isoflurane were administered the indicated AAV9 vector dose of AAV9-*AMPKγ1* (5×10^{11} vg, 200 μL), AAV9-$AMPK\gamma1^{K234R}$ (5×10^{11} vg, 200 μL), or AAV9-*VCPIP1* (5×10^{11} vg, 200 μL) by tail vein injection. Following cardiac functional assessment, mice were euthanized, and cardiac tissues along with blood samples were collected for subsequent analysis.

NPRCs, AMPCs, and cell lines

NRPCs isolation and cell culture. NRPCs were isolated from Sprague Dawley rat neonates. Briefly, the cardiac tissues were excised and immersed in phosphate-buffered saline (PBS) for blood removal. Ventricular tissue was dissected free from atrial tissue and then minced into 1 mm^3 fragments. Tissue digestion was performed using pancreatin and collagenase solution at 37 °C, involving 8 to 10 repetitions in 8 min cycles. After each digestion cycle, the supernatant was collected, with the initial digestate being discarded. Collected supernatants were pooled and in Dulbecco's modified Eagle's medium (DMEM; Gibco, Eggenstein, Germany) supplemented with 20% fetal bovine serum (FBS; Gibco). Following centrifugation ($1000 \times g$ for 10 min), the cellular pellet was resuspended in DMEM containing 10% FBS, passed through a 70 μm strainer, and transferred to a humidified 37 °C atmosphere supplied with 5% CO_2. After 2 h of incubation, the culture medium was collected and centrifuged at 1000 g for 10 min and replaced with a complete medium. Following 24 h of culture, adherent cardiomyocytes were subsequently utilized for further experimentation. NRCMs underwent an 8-h starvation period prior to being assigned to D-glucose (33 mM; Sigma-Aldrich) combined with palmitic acid (100 μM; Sigma-Aldrich) as the HG + PA group, and D-glucose (5.5 mM) as control group.

AMPCs were isolated and cultured as previously described[57] Briefly, following anesthesia, mice underwent thoracotomy for rapid heart excision and aortic cannulation. Hearts were sequentially perfused with EDTA buffer, perfusion buffer, and collagenase-containing digestion buffer until adequate tissue softening was achieved. The ventricles were then minced, gently triturated, and the digestion was stopped by adding the stop buffer. The crude cell suspension was passed through a 100 μm strainer, followed by gravity-based enrichment of the cardiomyocyte fraction. Following resuspension in fresh culture medium, cells were incubated at 37 °C under 5% CO_2 conditions.

HEK293T, AC16, and H9C2 cell lines were procured from the Shanghai Institute of Biochemistry and Cell Biology (Shanghai, China) and subsequently cultured in DMEM containing 10% FBS under standard conditions.

Gene knockdown and overexpression

The *Vcpip1*, *Tkt*, *Myo6*, *Prkag1*genes were silenced using VCPIP1 siRNA (5′-CCAUGAAUUUGCUACCUAATT-3′; and 5′-UUAGGUAGCAAAUUCAUGGTT-3′), TKT siRNA (5′-ACAUGGCUGAGCAGAUUAUTT-3′; and 5′-AUAAUCUGCUCAGCCAUGUTT-3′), MYO6 siRNA (5′-CCUGCACCUUGGAAAUAUUTT-3′; and 5′-AAUAUUUCCAAGGUGCAGGTT-3′), and AMPKγ1 siRNA (5′-CCACAGGCUUCCAGUUAUUTT-3′; and 5′-AAUAACUGGAAGCCUGUGGTT-3′), respectively. These oligonucleotides were synthesized by GenePharma (Shanghai, China). Additionally, plasmids of Flag-VCPIP1, His-AMPKα2, HA-AMPKγ1, HA-AMPKγ2, Flag-VCPIP1-delete ΔUBX-L and ΔOTU domain (Flag-VCPIP1-ΔUBX-L and Flag-VCPIP1-ΔOTU), VCPIP1 carrying the C218A mutation (Flag-VCPIP1-C218A), AMPKγ1 carrying the K100R, K234R, and K264R mutation (HA-AMPKγ1-K100R, HA-AMPKγ1-K234R, and HA-AMPKγ1-K264R) and HA-AMPKγ1-delete ΔCBS domain (HA-AMPKγ1-ΔCBS1, HA-AMPKγ1-ΔCBS2, HA-AMPKγ1-ΔCBS3, and HA-AMPKγ1-ΔCBS4) were obtained from Unibio (Chongqing, China). Transfection of siRNAs and plasmids into cells was performed using jetPRIME Reagent (Polyplus, Strasbourg, France).

$AMPK\gamma1^{-/-}$-H9C2 Cell Construction

A gRNA targeting the AMPKγ1 (*PRKAG1*) gene was cloned into lentiCas9-Blast (YouBio, Changsha, China). Lentiviral particles were generated by co-transfecting HEK 293T cells using three plasmids (psPAX2, pMD2.G, and lentiCas9-Blast-AMPKγ1 gRNA) for 48 h, followed by supernatant collection. H9C2 cells were then infected with the lentivirus-containing supernatant and selected with puromycin to obtain monoclonal cell lines. The efficiency of the AMPKγ1 knockout was validated through Western blot analysis The gRNA sequences targeting AMPKγ1 are provided in Supplementary Table 4.

Echocardiography

Echocardiographic assessment was performed on mice sedated with 2%-2.5% isoflurane and placed on a platform without mechanical ventilation. Images were acquired using a multimode small animal ultrasound imaging system (VINNO Technology, Suzhou, China). Long-axis M-mode echocardiography was obtained at the mitral valve tip level, while diastolic function was assessed from four-chamber views. The EF was determined based on the following equation: EF% = [LVEDV-LVESV/LVEDV] × 100%. FS was calculated as FS% = [LVEDD- LVEDS/LVEDD] × 100%.

Histological staining

Paraffin-embedded heart sections were stained with H&E (G1120, Solarbio, Beijing, China), Sirius Red (G3632, Solarbio), or Masson's Trichrome (G1340, Solarbio) for histopathological analysis. Subsequently, slides of myocardial pathological changes were observed under random fields using a light microscope (200× magnification; Leica, Wetzlar, Germany) and quantified with ImageJ (National Institutes of Health, Bethesda, USA).

To quantify cardiomyocyte hypertrophy, paraffin-embedded heart tissue sections were stained using a WGA staining kit (C1610, Solarbio). The samples were observed under random fields using a fluorescence microscope.

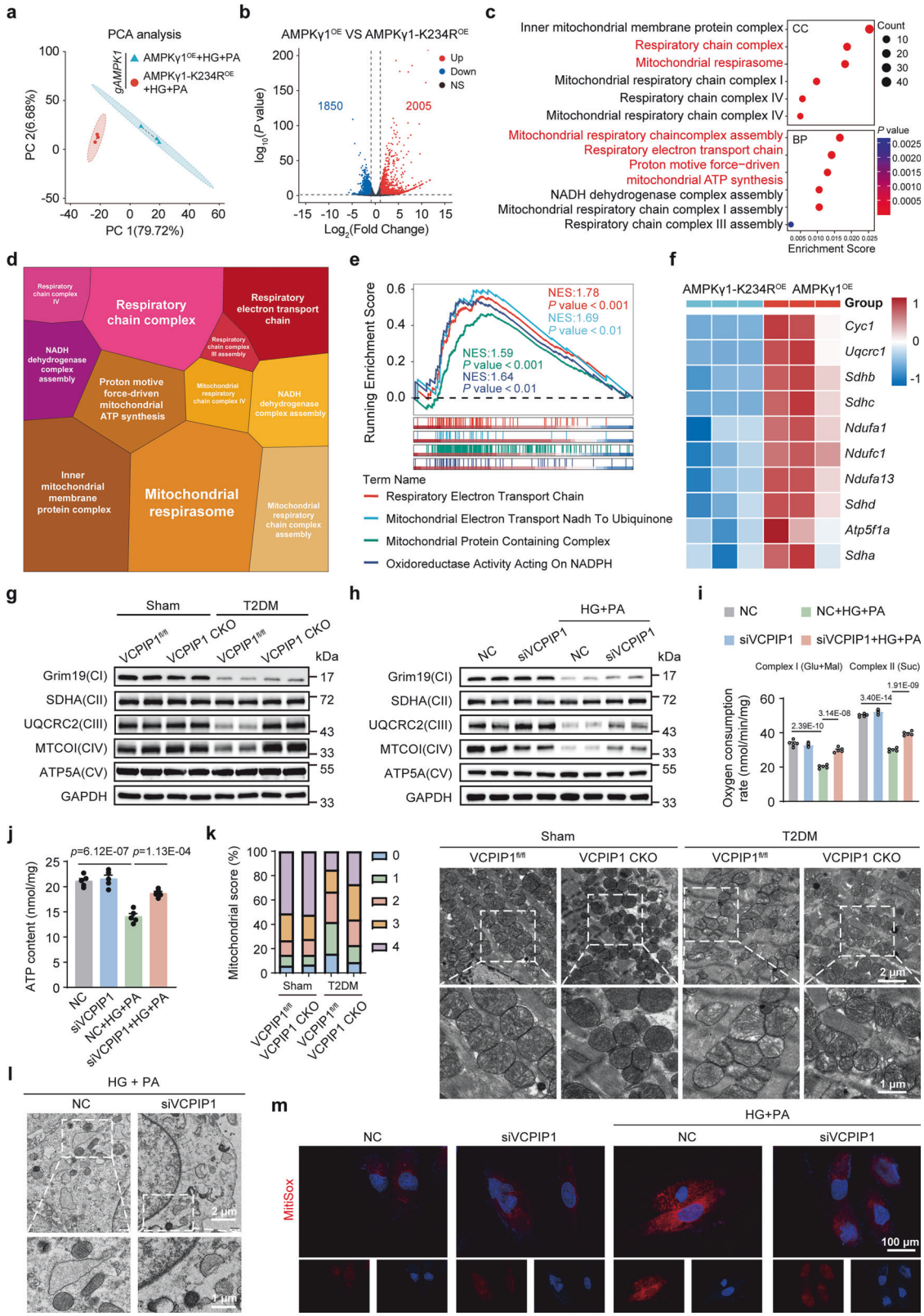

Real-time quantitative PCR (RT-qPCR)

Total RNA was extracted utilizing RNAiso Plus (Takara, Tokyo, Japan). Subsequently, exactly 1 μg of the RNA was reverse transcribed into cDNA with the Hifair® III 1st Strand cDNA Synthesis SuperMix (YEASEN, Shanghai, China). Quantitative amplification was then executed on a Bio-Rad CFX96 Touch Real-Time PCR Detection System (Bio-Rad, California, USA) formulated with SYBR Green Master Mix (YEASEN). All primers, provided by Sangon Biotech (Shanghai, China), are detailed in Supplementary Table 5. *β-actin* served as an internal control for normalization.

Fig. 7 VCPIP1-mediated AMPKγ1 deubiquitination impairs cardiac mitochondrial OXPHOS in diabetic cardiomyocytes. **a** A bulk RNA-sequencing was performed on AMPKγ1-deficient H9C2 cells transfected with either AMPKγ1 plasmid (AMPKγ1^{OE}) or AMPKγ1-K234R plasmid (AMPKγ1-K234R^{OE}). Principal-component analysis (PCA) visualized the transcriptomic separation of the two groups. **b** Volcano plot depicted differentially expressed genes (DEGs) between the two groups. **c**, **d** Gene Ontology (GO) analysis of upregulated DEGs in the cellular component (CC) and biological process (BP) categories. **e** Gene Set Enrichment Analysis (GSEA) related to mitochondrial respiratory chain complex and mitochondrial respirasome. **f** Heat map of the mitochondrial respirasome-related DEGs between two groups. **g** Western blot analysis and densitometric quantification of mitochondrial respiratory chain complex proteins (Grim19, SDHA, UQCRC2, MTCO1, and ATP5A) in heart tissues from sham and T2DM mice in both VCPIP1$^{fl/fl}$ and VCPIP1 conditional knockout (CKO) groups. **h** Primary cardiomyocytes transfected with siVCPIP1 or scrambled negative control (NC) were exposed to high glucose (HG; 33 mM) and palmitic acid (PA; 100 μM) for 24 h. Respiratory-chain proteins were examined by Western blotting. **i** Oxygen consumption by mitochondrial complex I and complex II in mitochondria isolated from primary cardiomyocytes. **j** The ATP content was detected in primary cardiomyocytes. **k** Representative images of transmission electron microscopy illustrated mitochondrial morphology and quantitative analysis of mitochondrial morphology scores in heart tissues from each group of mice. **l** Primary cardiomyocytes transfected with siVCPIP1 or NC were stimulated with HG combing PA. Representative images of transmission electron microscopy illustrated mitochondrial morphology. **m** Representative images of MitoSOX staining in primary cardiomyocytes. For (**k**, **l**), scale bar = 1 and 2 μm; For **m**, scale bar = 100 μm. Data are shown as mean ± SEM; **h**–**j**, and **l**,**m**: $n = 5$; **a**–**g** and **k**: $n = 6$; P values were determined by one-way ANOVA followed by Tukey post hoc tests; P values indicated

Transcriptome sequencing

Transcriptomics study was conducted employing bulk RNA-sequencing. Total RNA was extracted from AMPKγ1-deficient H9C2 cells transfected with either AMPKγ1 plasmid (AMPKγ1^{OE}) or AMPKγ1-K234R expression plasmid (AMPKγ1-K234R^{OE}) and subsequently challenged with HG + PA, using TRIzol reagent (Invitrogen, Carlsbad, CA, USA). The RNA concentration of samples was determined via a spectrophotometer (NanoDrop, Wilmington, DE, USA), and the sample purity was assessed utilizing an Agilent 2100 Bioanalyzer (Thermo Fisher Scientific, Waltham, MA, USA). Next, mRNA was isolated from 1 μg of total RNA using Oligo(dT)-attached magnetic beads. The purified mRNA was then fragmented into small pieces using a fragmentation buffer at an optimal temperature. Subsequently, reverse transcription was performed with random hexamer primers to convert the fragments of RNA into cDNA. Subsequent cDNA library construction and sequencing were carried out on the BGISEQ-500 platform (Beijing Genomics Institute, Shenzhen, China). Clean sequencing reads were aligned to the rat reference genome utilizing the combined Bowtie2 (version 2.2.5) and HISAT2 (version 2.0.4) algorithms. Transcript abundances were calculated as fragments per kilobase of exon per million mapped reads (FPKM) by applying the RSEM tool (version 1.2.12). Differential expression was statistically evaluated implementing the DESeq2 package in R, defining significance thresholds at an $P < 0.05$ and $|\mathrm{Log_2\ FC}| > 1$. Pathway enrichment analysis and GSEA were calculated using the GO database, with $P < 0.05$ and normalized enrichment score >1 set as significant.

Publicly available datasets were used including the GSE106177[58] and GSE197999[59] datasets from the GEO database. Within the R environment, the initial matrices underwent standard preprocessing steps, encompassing background correction, normalization, and data summarization. Platform-specific annotation files guided the translation of microarray probes into official gene symbols. During this mapping phase, unannotated probe sets were discarded, whereas expression matrices for genes targeted by multiple probe sets were collapsed by taking the average value. Finally, the DESeq2 package was similarly deployed to screen for DEGs within these public cohorts.

Immunofluorescence staining

Frozen sections (6 μm thickness) were obtained using a cryostat microtome (CryoStar NX70, Epredia, Shanghai, China). Slides underwent three PBS rinses with gentle agitation between washes. Excess buffer was removed by tapping, and the tissue margins were delineated using an IHC pen. Cells cultured in a 24-well plate for cellular immunofluorescence staining. After three PBS rinses, cells were fixed with 4% paraformaldehyde. Subsequently, fixed cell slides were washed with PBS and permeabilized with 0.1% Triton X-100. Then, all samples were blocked with 5% bovine serum albumin (BSA) for 1 h at the appropriate temperature and carried out using a four-color fluorescence kit (RC0086, Recordbio Biological Technology, Shanghai, China) via tyramide signal amplification (TSA) technology, following the provided instructions. The samples were incubated overnight at 4 °C with primary antibodies for VCPIP1 (1:100 dilution; sc-515291, Santa, Clara, USA), AMPKγ1 (1:100 dilution; 4187S, Cell Signaling Technology, MA, USA), TOM20 (1:100 dilution; 11802-1-AP, Proteintech, Wuhan, China), and α-actinin (1:100 dilution; ab137346, Abcam, Cambridge, UK), and subsequently treated with secondary antibodies including Cy3-conjugated goat anti-rabbit IgG (1:300 dilution; GB21303, Servicebio, Wuhan, China), Alexa Fluor® 488-conjugated goat anti-rabbit IgG (1:300 dilution; GB25303, Servicebio), and HRP labeled goat anti mouse IgG (1:300 dilution; GB23301, Servicebio) for 1 h at room temperature. After washing with PBS, the samples were incubated in TSA reaction buffer for 10 min, rinsed three times with PBS again, and finally counterstained with DAPI. Images were captured by using a confocal microscope (A1R-SIM-STORM, Nikon, Japan).

TRITC-Phalloidin staining

Cells cultured in glass-bottom dishes were fixed using 10% paraformaldehyde for 10 min. Then, the sample was stained with Actin-Tracker Red-Rhodamine (100 nM; C2207S, Beyotime, Shanghai, China) for 1 h at room temperature in a dark environment. Nuclear counterstaining was subsequently achieved utilizing a DAPI solution (C1005, Beyotime). The fluorescent images were acquired via an microscope (Leica).

MitoSOX fluorescence staining

Mitochondrial ROS levels were assessed in NRCMs with MitoSOX™ Red (M36008, Thermo Fisher Scientific) staining. Briefly, cells were incubated with fresh 5 μM MitoSOX staining at 37 °C in the dark for 30 min. The slides were counterstained with DAPI (Beyotime), and images were captured with a confocal microscope. Quantitative analysis of the fluorescence intensity within the images was performed with ImageJ (NIH) software.

In Situ PLA

Protein–protein interactions were detected using the Duolink In Situ Red Starter Kit Mouse/Rabbit (Sigma-Aldrich; DUO92101). Following blocking at 37 °C, cells were incubated overnight with primary antibodies: rabbit anti-AMPKγ1 (1:200 dilution; 4187S, Cell Signaling Technology) and mouse anti-VCPIP1 (1:200 dilution; sc-515291, Santa). Subsequently, samples were washed in Duolink In Situ Wash Buffer A and incubated with Duolink PLA probes (Duolink In Situ PLA Probe Anti-Rabbit PLUS and Duolink In Situ PLA Probe Anti-Mouse MINUS) for 60 min. Ligation was performed for 30 min, followed by amplification for 100 min using Duolink reagents. Samples were then washed in Duolink In Situ Wash Buffer B and counterstained with DAPI. Images were acquired and analyzed by fluorescence microscopy.

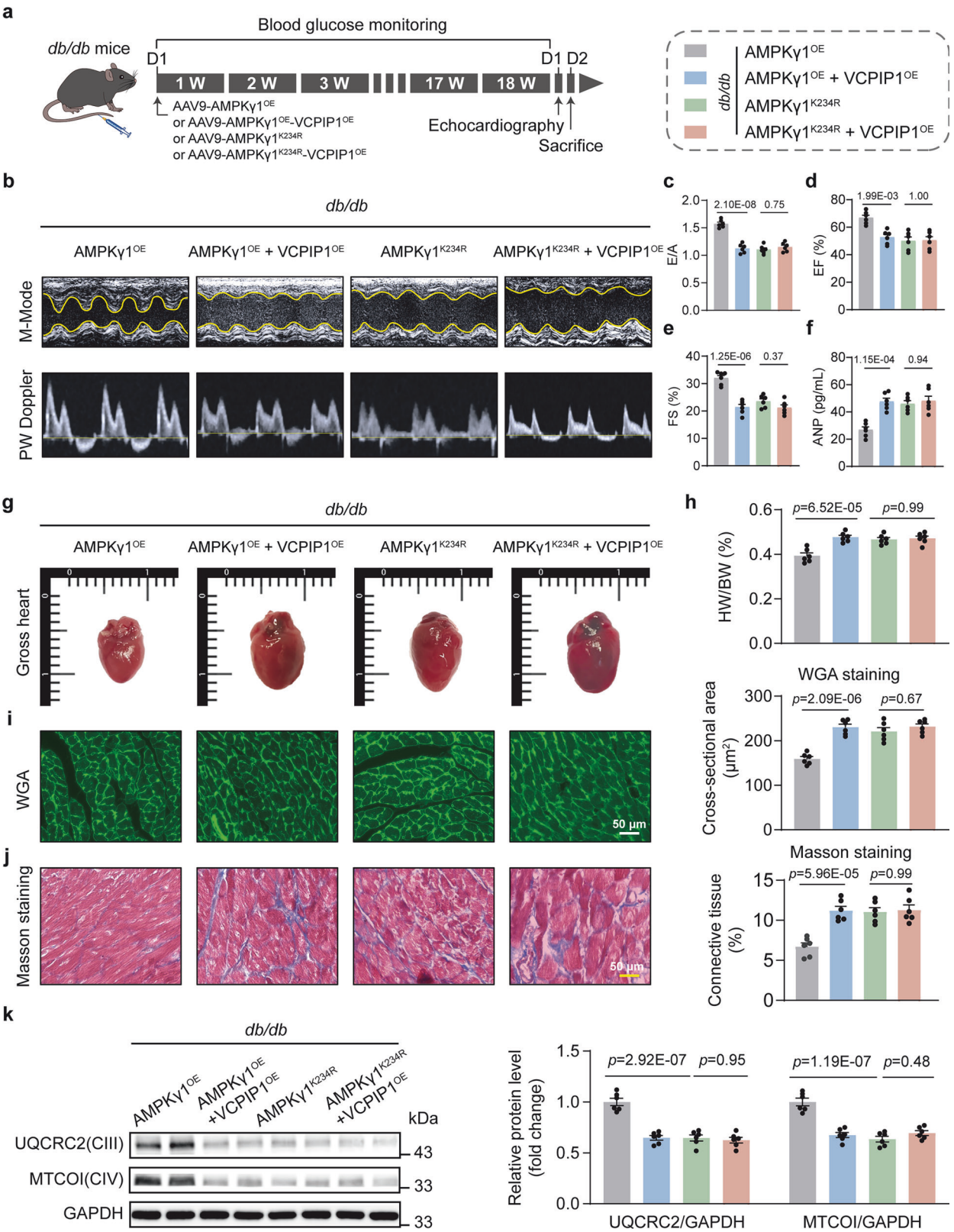

Fig. 8 AMPKγ1-K234R mutation phenocopies VCPIP1-mediated DCM in *db/db* mice. **a** Adeno-Associated Virus 9 (AAV9) vectors carrying AMPKγ1 (AMPKγ1^{OE}), AMPKγ1-K234R (AMPKγ1^{K234R}), and VCPIP1 (VCPIP1^{OE}) with the cardiomyocyte-specific promoter *cTNT* were administered to *db/db* mice via tail vein injection. **b** Representative images of echocardiography in each group. **c**–**e** Values of E to A peak velocity ratio (E/A), ejection fraction (EF%), and fractional shortening (FS%) by echocardiography. **f** Serum levels of atrial natriuretic peptide (ANP) in each group. **g** Representative images of whole heart. **h** The ratio of heart weight to body weight (HW/BW). **i** Wheat germ agglutinin (WGA) staining and quantitative analysis in heart sections. **j** Representative images and quantification of Masson's Trichrome in heart tissues. **k** Western blot analysis of mitochondrial respiratory chain complex proteins (UQCRC2, MTCO1) in heart tissues. For **I**, **j**, scale bar = 50 μm. Data are shown as mean ± SEM; $n = 6$; *P* values were determined by one-way ANOVA followed by Tukey post hoc tests; *P* values indicated

Transmission electron microscopy (TEM) analysis
The mitochondrial morphology was analyzed using TEM (HT7800, Hitachi, Tokyo, Japan). Briefly, left ventricular tissue samples measuring 1.0 mm^3 and cells were fixed in a solution containing 1.25% glutaraldehyde and 0.1 M sodium cacodylate buffer overnight. The fixed samples then underwent sequential dehydration in ethanol followed by epoxy resin embedding. Subsequently, ultrathin sections (90 nm) were prepared and stained with uranyl acetate and lead citrate before being observed. TEM examination at higher magnification revealed mitochondrial damage. Representative images were acquired to document the characteristic mitochondrial abnormalities observed in diabetic cardiac tissue. Digital images were analyzed to evaluate morphological parameters of mitochondrial damage.

ATP detection
ATP concentrations were evaluated by an ATP assay kit (S0026, Beyotime). Samples were disrupted in lysis buffer. Lysates were centrifuged at 12,000 × *g* for 5 min at 4 °C. The resulting supernatant was transferred to a 96-well plate and mixed with ATP detection reagent. ATP content was recorded using a luminometer.

Oxygen consumption measurements
Mitochondria were isolated from NRPCs and AMPCs. Cells were washed in PBS containing 10 mM EDTA, digested with trypsin, and homogenized in medium A (1 mM EDTA, 0.32 M sucrose, and 10 mM Tris22 base, pH 7.4). Mitochondrial protein concentration was determined using the BCA Protein Assay Kit (Beyotime). Oxygen consumption was assessed using a Clark-type oxygen electrode (Oroboros Instruments, Innsbruck, T, Austria). Complex I activity was stimulated by the substrates including 1 M glutamate and 1 M malate (5:1), and inhibited by 1 mM rotenone after baseline levels off. Complex II activity was induced by the substrate succinate (1 M) and stopped with 10 μM antimycin A. The oxygen consumption rates were recorded.

LC-MS/MS analysis
To investigate VCPIP1-binding proteins in cells, cardiomyocytes were transfected with either Flag-VCPIP1 or Flag-EV plasmid with HG + PA treatment. Cells were harvested using lysis buffer and incubated with anti-Flag and protein G-Sepharose beads at 4 °C overnight. The protein mixtures bound to the beads were extracted using SDT lysate (4% SDS, 100 mM DTT, 100 mM Tris-HCl) and then digested into peptides via filter-aided sample preparation (FASP) method. The LC-MS/MS was performed by PTM Bio (Hangzhou, China).

LC-MS/MS for ubiquitinated proteins
Cardiomyocytes were transfected with either Flag-VCPIP1 or Flag-EV plasmid for ubiquitin proteomics analysis. For each sample, the protein was reduced with 5 mM dithiothreitol at 56 °C for 30 min and subsequently alkylated with 11 mM iodoacetamide under light-protected conditions. The proteins were first digested with trypsin at a 1:50 trypsin-to-protein ratio overnight, succeeded by a secondary cleavage at a 1:100 ratio for 4 h at 37 °C. The resulting peptides were divided for ubiquitin peptide enrichment (95%) and protein quantification (5%). For ubiquitin remnant enrichment, peptides were dissolved in NETN buffer and incubated with pre-washed antibody beads (PTM-1104, PTM Bio) at 4 °C overnight with gentle agitation. LC-MS/MS analysis and subsequent integrated ubiquitinome and proteome profiling were conducted by PTM Bio.

Western blotting
The samples were split by sodium dodecyl sulfate-polyacrylamide gel electrophoresis (SDS-PAGE) and then transferred to polyvinylidene difluoride (PVDF) membranes (Millipore, Billerica, USA). The PVDF membranes were blocked with 5% nonfat milk for 1 h at room temperature and subsequently incubated with the primary antibody against AMPKγ1 (A22024, ABclonal, Wuhan, China), AMPK (2532S, Cell Signaling Technology), VCPIP1 (sc-515291, Santa), p^{T172}-AMPK (50081, Cell Signaling Technology), ANP (sc-515707, Santa), MyHC (sc-376157, Santa), Flag-tag antibody (AE063, ABclonal), HA-tag antibody (51064-2-AP, Proteintech, Wuhan, China), Grim19 (sc-365978, Santa), SDHA (ab14715, Abcam), UQCRC2 (ab14745, Abcam), MTCO1 (ab14705, Abcam), ATP5A (ab14748, Abcam), ACC (3662S, Cell Signaling Technology), p-ACC (3661S, Cell Signaling Technology), mTOR (#2983, Cell Signaling Technology), p-mTOR (#2971, Cell Signaling Technology), and GAPDH (60004-1-Ig, Proteintech). Following washed with Tris buffered saline (TBS)-Tween buffer, membranes were visualized by incubation with an HRP-conjugated secondary antibody and performed using a chemiluminescence kit (G2014, Servicebio). Image intensities were photographed with Chemiluminescence and fluorescence imaging systems (Clinx Science Instruments) and assessed by ImageJ software (NIH).

Co-IP
For Co-IP experiments, the corresponding primary antibody was incubated with 70 μL of Protein A + G Agarose beads (P2012, Beyotime) on a vibrator at 4 °C for 6 h. The cell lysates were then added to the beads and incubated overnight on a vibrator at 4 °C. After centrifugation for 5 min at 3000 g, the supernatant was discarded. Subsequently, the magnetic bead was washed five times with PBS to remove unbound proteins, and protein loading buffer (2×) was added to elute the proteins. The proteins were resolved on SDS-PAGE, transferred to PVDF membranes, and analyzed with immunoblotting. The primary antibodies used in this experiment included Flag-tag antibody (AE063, ABclonal), HA-tag antibody (51064-2-AP, Proteintech), Myc-tag antibody (16286-1-AP, Proteintech), p^{T172}-AMPK (50081, Cell Signaling Technology), LKB1 (10746-1-AP, Proteintech), AMPKγ1 (A22024, ABclonal), VCPIP1 (sc-515291, Santa), K48-linkage Specific Polyubiquitin Antibody (#4289, Cell Signaling Technology), K63-linkage Specific Polyubiquitin Antibody (#5621, Cell Signaling Technology), and GAPDH (60004-1-Ig, Proteintech).

Deubiquitination assay
HEK293T cells were co-transfected with Myc-tagged ubiquitin for K48- or K63- specific linkage, Flag-tagged VCPIP1, and HA-tagged AMPKγ1 and subsequently treated with MG132 (T2154, TargetMol, Boston, USA) to enhance the level of ubiquitinated AMPKγ1. Immunoprecipitation was executed to isolate ubiquitinated AMPKγ1, which was captured via anti-HA antibodies and protein G beads. The beads were rinsed three times with cell lysis buffer for western and IP and incubated with Flag-VCPIP1 proteins. The complexes were evaluated by immunoblotting.

BLI
The binding affinities between recombined human recombined protein VCPIP1 and AMPK were identified by BLI assay using the Octet Red instrument (ForteBio, Fremont, USA). All proteins were prepared in PBS. Briefly, VCPIP1 was loaded onto Dip and Read Anti-Human IgG biosensors (ForteBio) and equilibrated with PBS. The biosensors were then subjected to AMPK, followed by rinsing with PBS. Kinetic modeling was executed using the Fortebio Octet Data analysis software.

Statistical analysis
Data were presented as the mean ± standard error of the mean (SEM) derived from at least three independent experiments. All statistical evaluations were executed utilizing GraphPad Prism 8.01 (GraphPad, CA, USA). For evaluating differences between two cohorts, an unpaired two-tailed Student's *t* test was employed for normally distributed variables with equal variance, Welch's *t*-test

was utilized for normally distributed variables with unequal variance, and the Mann-Whitney U test was conducted for non-normal distributed metrics; For assessing multiple groups of variables, a one-way analysis of variance (ANOVA) followed by Tukey's multiple comparisons test was implemented for normally distributed metrics with equal variance, and the Kruskal-Wallis test incorporating Dunn post hoc tests was executed to analyze datasets exhibiting unequal variance and non-normal distribution. A one-way ANOVA followed by a multiple comparisons test with Tukey was utilized to evaluate the variations. $P < 0.05$ was deemed statistically significant.

DATA AVAILABILITY

The raw bulk RNA sequencing data generated in this study have been deposited in the Sequence Read Archive (SRA) under BioProject accession number PRJNA1300341. The publicly available single-cell RNA sequencing and bulk RNA sequencing datasets analyzed in this study are accessible in the Gene Expression Omnibus (GEO) database under the following accession numbers GSE290932, GSE197999, and GSE106177. The raw ubiquitin proteome mass spectrometry data generated in this study are available in the jPOST database under accession code JPST003971. The raw data of mass spectrometry is available at the PRIDE database under dataset identifier PXD067421. All data included within the article or Supplementary Information are available from the authors on request. The study materials and analytical methods are also available from the corresponding author on reasonable request.

ACKNOWLEDGEMENTS

This study was supported by the National Natural Science Foundation of China (U24A20814 to G.L.), the Key Discipline of Zhejiang Province in Public Health and Preventive Medicine (First Class, Category A) at Hangzhou Medical College, the Medical Scientific Research Foundation of Zhejiang Province (Grants No. 2024KY932 to X.H.), the Basic Scientific Research Funds of Department of Education of Zhejiang Province (Grants No. KYZD2025004 to X.H.), and the Zhejiang Provincial Traditional Chinese Medicine Science and Technology Program Project (grant no. 2026ZL0088 to X.H.). The authors acknowledge the support from the Scientific Research Center, Hangzhou Medical College, and Liwei, Laboratory Animal Center of Zhejiang University, for her assistance in animal experiments.

AUTHOR CONTRIBUTIONS

X.H., Z.H., and G.L. drafted and revised the manuscript; X.H., Z.H., W.L., Y.L., G.L., J.Z., J.T., M.H., Y.W., and Z.L. designed and performed the experiments. J.Z, M.H., and W.L generated cardiomyocyte-specific VCPIP1 knockout mice. G.L., H.Y., and Q.S. supervised the work. All authors approved the final version of the manuscript.

ADDITIONAL INFORMATION

Supplementary information The online version contains supplementary material available at https://doi.org/10.1038/s41392-026-02701-9.

Competing interests: The authors declare no competing interests.

Publisher's note Springer Nature remains neutral with regard to jurisdictional claims in published maps and institutional affiliations.

REFERENCES

1. Saeedi, P. et al. Global and regional diabetes prevalence estimates for 2019 and projections for 2030 and 2045: results from the International Diabetes Federation Diabetes Atlas, 9th edition. *Diab. Res. Clin. Pract.* **157**, 107843 (2019).
2. Fernandez, C. J., Shetty, S. & Pappachan, J. M. Diabetic cardiomyopathy: emerging therapeutic options. *World J. Diab.* **15**, 1677–1682 (2024).
3. Bouthoorn, S. et al. The prevalence of left ventricular diastolic dysfunction and heart failure with preserved ejection fraction in men and women with type 2 diabetes: a systematic review and meta-analysis. *Diab. Vasc. Dis. Res.* **15**, 477–493 (2018).
4. Tan, Y. et al. Mechanisms of diabetic cardiomyopathy and potential therapeutic strategies: preclinical and clinical evidence. *Nat. Rev. Cardiol.* **17**, 585–607 (2020).
5. Seferović, P. M. et al. Diabetic myocardial disorder. A clinical consensus statement of the Heart Failure Association of the ESC and the ESC Working Group on Myocardial & Pericardial Diseases. *Eur. J. Heart Fail.* **26**, 1893–1903 (2024).
6. Moka, M. K., K, S. D. & George, M. Emerging clinical approaches in diabetic cardiomyopathy: insights from clinical trials and future directions. *Acta Diabetol.* **62**, 1–10 (2025).
7. Cai, W., Chong, K., Huang, Y., Huang, C. & Yin, L. Empagliflozin improves mitochondrial dysfunction in diabetic cardiomyopathy by modulating ketone body metabolism and oxidative stress. *Redox Biol.* **69**, 103010 (2024).
8. Li, B. et al. FARS2 deficiency causes cardiomyopathy by disrupting mitochondrial homeostasis and the mitochondrial quality control system. *Circulation* **149**, 1268–1284 (2024).
9. Peng, C., Zhang, Y., Lang, X. & Zhang, Y. Role of mitochondrial metabolic disorder and immune infiltration in diabetic cardiomyopathy: new insights from bioinformatics analysis. *J. Transl. Med.* **21**, 66 (2023).
10. Yan, M. et al. Mitochondrial damage and activation of the cytosolic DNA sensor cGAS-STING pathway lead to cardiac pyroptosis and hypertrophy in diabetic cardiomyopathy mice. *Cell Death Discov.* **8**, 258 (2022).
11. Tocchetti, C. G. et al. GSH or palmitate preserves mitochondrial energetic/redox balance, preventing mechanical dysfunction in metabolically challenged myocytes/hearts from type 2 diabetic mice. *Diabetes* **61**, 3094–3105 (2012).
12. Han, X. et al. Cardiomyocyte PRL2 promotes cardiac hypertrophy via directly dephosphorylating AMPKα2. *Circ. Res.* **136**, 645–663 (2025).
13. Zhang, Y. et al. Melatonin attenuates myocardial ischemia-reperfusion injury via improving mitochondrial fusion/mitophagy and activating the AMPK-OPA1 signaling pathways. *J. Pineal Res.* **66**, e12542 (2019).
14. Wang, L. et al. Endurance exercise preconditioning alleviates ferroptosis induced by doxorubicin-induced cardiotoxicity through mitochondrial superoxide-dependent AMPKα2 activation. *Redox Biol.* **70**, 103079 (2024).
15. Karbassi, E. et al. Cardiomyocyte maturation: advances in knowledge and implications for regenerative medicine. *Nat. Rev. Cardiol.* **17**, 341–359 (2020).
16. Seymour, L. et al. Roles of post-translational modifications of transcription factors involved in breast cancer hypoxia. *Molecules* **30**, 645 (2025).
17. Liu, X. et al. Deubiquitinase JOSD2 alleviates colitis by inhibiting inflammation via deubiquitination of IMPDH2 in macrophages. *Acta Pharm. Sin. B* **15**, 1039–1055 (2025).
18. Zeng, L. et al. Ubiquitin proteasome system in cardiac fibrosis. *J. Adv. Res.* **S2090-1232**, 00562–00569 (2024).
19. Ye, B. et al. USP25 ameliorates pathological cardiac hypertrophy by stabilizing SERCA2a in cardiomyocytes. *Circ. Res.* **132**, 465–480 (2023).
20. Han, J. et al. Cardiomyocyte-derived USP28 negatively regulates antioxidant response and promotes cardiac hypertrophy via deubiquitinating TRIM21. *Theranostics* **14**, 6236–6248 (2024).
21. Xie, S. Y. et al. USP28 serves as a key suppressor of mitochondrial morphofunctional defects and cardiac dysfunction in the diabetic heart. *Circulation* **149**, 6684–6706 (2024).
22. Kang, N. et al. Identification and characterization of host factor VCPIP1 as a multifunctional positive regulator of hepatitis B virus. *J. Virol.* **98**, e0158124 (2024).
23. Liao, T. et al. Molecular basis of VCPIP1 and P97/VCP interaction reveals its functions in post-mitotic golgi reassembly. *Adv. Sci.* **11**, e2403417 (2024).
24. Liu, Z. et al. VCPIP1 facilitates pancreatic adenocarcinoma progression via Hippo/YAP signaling. *Cell Death Dis.* **16**, 422 (2025).
25. Huang, J. et al. Tandem deubiquitination and acetylation of SPRTN promotes DNA-protein crosslink repair and protects against aging. *Mol. Cell* **79**, 824–835.e5 (2020).
26. Jeon, Y. H. et al. Adiponectin enhances the bioenergetics of cardiac myocytes via an AMPK- and succinate dehydrogenase-dependent mechanism. *Cell. Signal.* **78**, 109886 (2021).
27. Yan, G. et al. Integrated stress response potentiates ponatinib-induced cardiotoxicity. *Circ. Res.* **134**, 482–501 (2024).
28. Eibach, Y. et al. The deubiquitinase USP5 prevents accumulation of protein aggregates in cardiomyocytes. *Sci. Adv.* **11**, eado3852 (2025).
29. Erkut, E. et al. A cardiovascular, craniofacial, and neurodevelopmental disorder caused by loss-of-function variants in the eIF3 complex component genes EIF3A and EIF3B. American journal of human genetics. *Am. J. Hum. Genet.* **112**, 2625–2642 (2025).
30. Karatsai, O. et al. Unconventional myosin VI in the heart: involvement in cardiac dysfunction progressing with age. *Biochim. Biophys. Acta Mol. Basis Dis.* **1869**, 166748 (2023).
31. Liang, Q. Z. et al. Integration of multi-omics and machine learning strategies identifies immune related candidate biomarkers in inflammation-associated hypertrophic cardiomyopathy. *Front. Immunol.* **16**, 1645382 (2025).
32. Han, X. et al. Cardiomyocyte OTUD1 drives diabetic cardiomyopathy via directly deubiquitinating AMPKα2 and inducing mitochondrial dysfunction. *Nat. Commun.* **16**, 6668 (2025).
33. Arad, M. et al. Transgenic mice overexpressing mutant PRKAG2 define the cause of Wolff-Parkinson-White syndrome in glycogen storage cardiomyopathy. *Circulation* **107**, 2850–2856 (2003).

34. Kim, M. et al. Mutation in the γ2-subunit of AMP-activated protein kinase stimulates cardiomyocyte proliferation and hypertrophy independent of glycogen storage. *Circ. Res.* **114**, 966–975 (2014).
35. Wu, S. & Zou, M. H. AMPK, mitochondrial function, and cardiovascular disease. *Int. J. Mol. Sci.* **21**, 4987 (2020).
36. Yan, Y., Zhou, X. E., Xu, H. E. & Melcher, K. Structure and physiological regulation of AMPK. *Int. J. Mol. Sci.* **19**, 3534 (2018).
37. Liu, F. et al. Ubiquitination and deubiquitination in cancer: from mechanisms to novel therapeutic approaches. *Mol. Cancer* **23**, 148 (2024).
38. Zhao, Q. et al. The deubiquitinase OTUB1 inhibits gluconeogenesis by stabilizing YWHAB. *Cell. Signal.* **124**, 111408 (2024).
39. Zhong, L. et al. Cardiomyocyte-enriched USP20 ameliorates pathological cardiac hypertrophy by targeting STAT3 deubiquitination. *Adv. Sci.* **12**, e2416478 (2025).
40. Ye, B. et al. Deubiquitinase USP25 alleviates obesity-induced cardiac remodeling and dysfunction by downregulating TAK1 and reducing TAK1-mediated inflammation. *JACC Basic Transl. Sci.* **9**, 1287–1304 (2024).
41. Han, J. et al. Deubiquitinase JOSD2 improves calcium handling and attenuates cardiac hypertrophy and dysfunction by stabilizing SERCA2a in cardiomyocytes. *Nat. Cardiovasc. Res.* **2**, 764–777 (2023).
42. Yan, M. et al. USP7 promotes cardiometabolic disorders and mitochondrial homeostasis dysfunction in diabetic mice via stabilizing PGC1. *Pharmacol. Res.* **205**, 107235 (2024).
43. Li, J. T. et al. Dietary folate drives methionine metabolism to promote cancer development by stabilizing MAT IIA. *Signal Transduct. Target. Ther.* **7**, 192 (2022).
44. Tsai, Y. C. et al. Deubiquitinating enzyme VCIP135 dictates the duration of botulinum neurotoxin type A intoxication. *Proc. Natl. Acad. Sci. USA* **114**, E5158–E5166 (2017).
45. Zuo, J. et al. VCPIP1 negatively regulates NF-κB signaling pathways by deubiquitinating and stabilizing Erbin in MDP-stimulated macrophages. *Int. Immunopharmacol.* **143**, 113622 (2024).
46. An, H. et al. The importance of the AMPK gamma 1 subunit in metformin suppression of liver glucose production. *Sci. Rep.* **10**, 10482 (2020).
47. Steinberg, G. R. & Carling, D. AMP-activated protein kinase: the current landscape for drug development. *Nat. Rev. Drug Discov.* **18**, 527–551 (2019).
48. Deng, M. et al. Deubiquitination and activation of AMPK by USP10. *Mol. Cell* **61**, 614–624 (2016).
49. Ritho, J., Arold, S. T. & Yeh, E. T. A critical SUMO1 modification of LKB1 regulates AMPK activity during energy stress. *Cell Rep.* **12**, 734–742 (2015).
50. Shin, H. J. et al. AMPK-SKP2-CARM1 signalling cascade in transcriptional regulation of autophagy. *Nature* **534**, 553–557 (2016).
51. Ovens, A. J. et al. Post-translational modifications of the energy guardian AMP-activated protein kinase. *Int. J. Mol. Sci.* **22**, 1229 (2021).
52. Lee, J. O. et al. E3 ubiquitin ligase, WWP1, interacts with AMPKα2 and downregulates its expression in skeletal muscle C2C12 cells. *J. Biol. Chem.* **288**, 4673–4680 (2013).
53. Qi, J. et al. Downregulation of AMP-activated protein kinase by Cidea-mediated ubiquitination and degradation in brown adipose tissue. *EMBO J.* **27**, 1537–1548 (2008).
54. Ross, F. A., Jensen, T. E. & Hardie, D. G. Differential regulation by AMP and ADP of AMPK complexes containing different γ subunit isoforms. *Biochem. J.* **473**, 189–199 (2016).
55. Madhavi, Y. V. et al. Targeting AMPK in diabetes and diabetic complications: energy homeostasis, autophagy and mitochondrial health. *Curr. Med. Chem.* **26**, 5207–5229 (2019).
56. Zhang, Y. et al. Mitochondrial aldehyde dehydrogenase 2 accentuates aging-induced cardiac remodeling and contractile dysfunction: role of AMPK, Sirt1, and mitochondrial function. *Free Radic. Biol. Med.* **71**, 208–220 (2014).
57. Ackers-Johnson, M. et al. A simplified, Langendorff-free method for concomitant isolation of viable cardiac myocytes and nonmyocytes from the adult mouse heart. *Circ. Res.* **119**, 909–920 (2016).
58. Hou, J. et al. Identification of hub genes and potential ceRNA networks of diabetic cardiomyopathy. *Sci. Rep.* **13**, 10258 (2023).
59. Xi, Y. et al. RNA sequencing of cardiac in a rat model uncovers potential target LncRNA of diabetic cardiomyopathy. *Front. Genet.* **13**, 848364 (2022).